energy&fuels

Compositional Control on Shale Pore Structure Characteristics across a Maturation Gradient: Insights from the Devonian New Albany Shale and Marcellus Shale in the Eastern United States

Bei Liu, Juan Teng,* Maria Mastalerz, Juergen Schieber, Arndt Schimmelmann, and David Bish

Cite This: https://doi.org/10.1021/acs.energyfuels.1c00526 Read Online

ABSTRACT: The pore structure characteristics of shales are controlled by their mineralogical and organic matter (OM) compositions. However, the contributions by different components in shales at varying thermal maturities remain poorly understood. In this study, Devonian New Albany Shale and Marcellus Shale samples spanning a thermal maturity from marginally mature (vitrinite reflectance R_o 0.55%) to post-mature (R_o 2.41%) were selected to study the control of the composition on the pore structure properties of shales at different stages of thermal maturation. Scanning electron microscopy (SEM) imaging was used to examine the pore types in shales, and low-pressure N_2 and CO_2 adsorption analyses were used to quantitatively characterize the mesopore and micropore characteristics of bulk shales and major components in shales. The results show that matrix-associated pores including interparticle pores between silt-sized mineral grains, phyllosilicate framework pores, and intraparticle pores within mineral grains exist in all samples but become less common with increasing maturity, which is likely caused by the elevated compaction, cementation, and occlusion with bitumen. Secondary organic pores were not observed by SEM at marginal maturity but were detected in the condensate-wet gas and dry gas windows, with more organic pores in the dry gas window. At marginal maturity, OM has large amounts of mesopores and micropores, as demonstrated by low-pressure N_2 and CO_2 adsorption analyses of OM isolated from shales, even though no OM-hosted pores were observed by SEM. With increasing thermal maturity, the mesopore and micropore specific surface areas (SSAs) of OM increase and make greater contributions to the pore structure properties of bulk shales. The mesopore and micropore properties of shales are controlled by the OM content and maturity as well as by the clay mineral type and content, and they can be estimated from the contribution of each component at different stages of thermal maturation. Accurate evaluation of the pore volume and SSA of shales will have important implications for assessing gas adsorption and transport in shales.

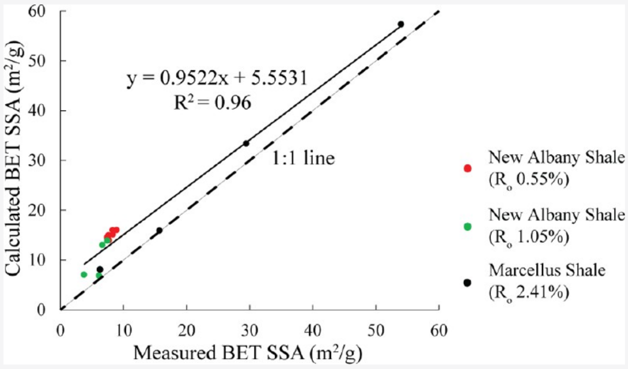

1. INTRODUCTION

Black shales serve as both a source rock and reservoir in unconventional petroleum systems.[1−6] Porosity and pore structure characteristics are important parameters in characterizing tight shale reservoir properties, which are controlled by organic and inorganic compositions of shales.[7−13] However, because of the abundance of clay minerals and organic matter (OM) in black shales and their evolution during thermal maturation,[9,14] the contribution of mineralogical and OM compositions to the pore structure of shales at different stages of thermal maturation is not well understood.

Pore spaces in tight shale reservoirs can be associated with the mineral matrix or hosted by OM.[15,16] Interparticle pores between mineral grains (e.g., quartz, feldspar, carbonate minerals, and clay mineral platelets) are a very important pore type because they have better interconnectivity and a relatively larger size than intraparticle pores and OM-hosted pores.[16,17] Interparticle and intraparticle pores in shales (tens to hundreds of nm in size) are no different from pores in conventional sandstone and carbonate reservoirs (several to tens of μm in size) except for their smaller sizes. Their formation and preservation are largely controlled by diagenetic processes.[14−16]

OM-hosted pores are an important constituent of the pore network in unconventional gas shales[15−19] and can be the dominant pore type in some shale plays.[16] The gas content and methane adsorption capacity of shales are largely controlled by total organic carbon (TOC) content,[7,20−22] suggesting that

Received: February 16, 2021
Revised: April 6, 2021

Table 1. Vitrinite Reflectance (R_o), Depth (m), TOC Content, and Mineralogical Composition of Shale Samples Determined by XRD[a]

				mineralogical composition by XRD (wt %)										
sample	R_o (%)	depth (m)	TOC (wt %)	quartz	feldspar	illite	chlorite	kaolinite	calcite	dolomite	pyrite	marcasite	gypsum	total clay
NAS-1	0.55	610.49	12.88	37 (1)	13 (2)	42 (2)	4 (1)	1 (0.5)		0.1 (0.1)	1.8 (0.1)	0.7 (0.1)		47 (4)
NAS-2	0.55	612.66	10.05	40 (1)	13 (2)	36 (1)	2 (0.5)	1 (0.5)		1 (1)	3.8 (0.1)	2.2 (0.1)	0.2 (0.1)	39 (2)
NAS-3	0.55	615.54	12.53	36 (1)	15 (2)	38 (1)	2 (0.5)	1 (1)		3 (1)	3.7 (0.1)	2.2 (0.1)		41 (3)
NAS-4	0.55	619.02	6.06	37 (1)	12 (2)	41 (1)	3 (0.5)	1 (0.5)		2 (1)	2.2 (0.1)	1.1 (0.1)	0.2 (0.2)	45 (2)
NAS-5	0.55	624.64	4.75	31 (1)	13 (2)	47 (1)	3 (0.5)	2 (0.5)		2 (1)	1.9 (0.1)	0.6 (0.1)	0.3 (0.2)	52 (2)
NAS-6	0.55	629.99	7.37	37 (1)	12 (1)	42 (1)	3 (0.5)	2 (0.5)		2 (1)	2.4 (0.1)	1.1 (0.1)	0.1 (0.1)	47 (2)
average	0.55	n.a.	8.98	36 (1)	13 (2)	41 (1)	3 (0.5)	1 (0.5)		2 (1)	2.6 (0.1)	1.3 (0.1)	0.1 (0.1)	45 (2)
HD-1	1.05	n.a.	6.52	46 (1)	16 (1)	28 (1)				7 (0.5)	2.4 (0.1)	1.5 (0.1)		28 (1)
HD-3	1.05	n.a.	3.64	70 (1)	10 (1)	11 (1)				4.5 (0.2)	4.1 (0.1)	0.7 (0.1)		11 (1)
HD-5	1.05	n.a.	7.12	46 (1)	15 (1)	30 (1)				4 (0.5)	2.5 (0.1)	1.6 (0.1)		30 (1)
HD-7	1.05	n.a.	3.47	65 (1)	9 (1)	12 (1)				4 (0.5)	8.6 (0.1)	1.2 (0.1)		12 (1)
average	1.05	n.a.	5.19	57 (1)	13 (1)	20 (1)				5 (0.5)	4.4 (0.1)	1.3 (0.1)		20 (1)
Mar-1	2.41	n.a.	1.64	4.1 (0.1)		3 (1)			93 (1)		0.8 (0.1)			3 (1)
Mar-2	2.41	n.a.	13.65	31 (1)	7 (2)	36 (2)		1 (0.5)	16 (0.5)	2 (0.5)	6.2 (0.1)	0.9 (0.1)	0.7 (0.1)	37 (3)
Mar-3	2.41	n.a.	8.36	38 (1)	4 (1)	12 (1)			44 (1)	0.5 (0.5)	1.7 (0.1)	0.4 (0.1)	0.6 (0.2)	12 (1)
Mar-4	2.41	n.a.	3.44	8.3 (0.1)	3 (0.5)	9 (1)			78 (1)	1.2 (0.1)	0.5 (0.05)		0.2 (0.1)	9 (1)
average	2.41	n.a.	6.77	20 (1)	4 (1)	15 (1)		0.5 (0.5)	58 (1)	1 (0.5)	2.3 (0.1)	0.3 (0.1)	0.4 (0.1)	15 (2)

[a] NAS series samples (R_o 0.55%) refer to the NAS from Daviess County, Indiana (Figure 1); HD series samples (R_o 1.05%) refer to the NAS from Hicks Dome, Illinois (Figure 1); Mar series samples (R_o 2.41%) refer to the Marcellus Shale from Canastota, New York (Figure 1). Minor muscovite is present in the NAS samples and was included in the illite fraction. Total clay = illite + kaolinite + chlorite. Feldspar is the sum of orthoclase, microcline, and albite. The numbers in the brackets refer to one-sigma-estimated standard deviations. n.a. = not applicable.

organic pores play an important role in methane storage in gas shales.

The size of OM-hosted pores is typically smaller than 1000 nm and can be as small as 1 nm or less.[9,15,16,20] OM-hosted pores are commonly imaged through observations of argon-ion-milled surfaces under scanning electron microscope (SEM).[15,16,23−25] However, SEM imaging can resolve only macropores (>50 nm) and mesopores (2−50 nm) and cannot characterize organic porosity quantitatively. Other techniques such as N_2 and CO_2 adsorption, molecular simulation, and small-angle and ultrasmall-angle neutron scattering can detect micropores (<2 nm) and allow quantitative evaluation.[7,9,26−29] Therefore, a significant portion of OM-hosted pores is SEM invisible,[19] and characterizing the full spectrum of organic pores requires a combination of qualitative SEM imaging and quantitative measurements.

Thermal maturity controls the evolution of mineralogical and organic components in shales during burial and consequently influences the reservoir properties of shales.[9,14,30−34] Oil-prone OM converts to oil, gas, solid bitumen (SB), or pyrobitumen during thermal maturation.[35−38] Other diagenetic processes that accompany OM maturation include clay mineral transformation (e.g., smectite to illite),[39] mechanical compaction, cementation, and mineral precipitation and dissolution, which together with OM maturation control the evolution of the pore network of shales during progressive burial.[14]

This study aims to quantitatively characterize the control of shale mineralogical and OM compositions on the pore structure characteristics of black shales based on a series of Devonian New Albany Shale (NAS) and Marcellus Shale samples from the eastern United States that span a thermal maturity range from vitrinite reflectance (R_o) 0.55 to 2.41%. Shale samples having the same thermal maturity but different TOC contents were used to study the contribution of organic pores to the pore structure of bulk shales. OM was isolated from black shales and analyzed by low-pressure N_2 and CO_2 adsorption. Adsorption analyses were also conducted on kaolinite and quartz silt. A comparison of the pore structure of bulk shales calculated on the basis of isolated OM, clay minerals, and quartz silt with the measured values should allow us to characterize the contributions of organic pores and mineral matrix-associated pores to the pore structure of black shales at different stages of hydrocarbon generation.

2. SAMPLES AND ANALYTICAL METHODS

2.1. Samples. Three sets of Devonian NAS and Marcellus Shale samples from the eastern United States were selected to study the control of the shale composition on their pore structure characteristics. Six NAS samples from drill core 1−3 Kavanaugh (NAS series in Table 1) from Daviess County, Indiana, USA,[40,41] and four NAS samples from the Hicks Dome (HD series in Table 1) of Hardin County, Illinois, USA, are marginally mature (R_o 0.5−0.6%) and within the condensate-wet gas window, respectively (Figure 1).[9,52] Because the highest maturity of the NAS is only R_o 1.5%,[9] four Marcellus Shale samples (Mar series in Table 1) from Canastota, New York, USA, that are in the dry gas window were selected to represent the high-maturity series (Figure 1).[53] Although the NAS and Marcellus Shale are from different basins, they have similar OM compositions[35,37] and clay mineral type, which have the most important control on mesopore and micropore properties of black shales.

OM was isolated from powdered shale samples through hydrochloric acid (HCl) and hydrofluoric acid (HF) demineralization and analyzed by low-pressure N_2 and CO_2 adsorption. Commercially available kaolinite (vendor Thiele Kaolin) and quartz silt (vendor US Silica) were used to evaluate the pore structure of inorganic components in shales.

2.2. Analytical Methods. *2.2.1. Organic Petrography.* Shale samples were crushed into rock chips that pass a 20-mesh sieve and made into whole-rock petrographic pellets following standard coal petrography procedures.[42] The mean random R_o values of shale

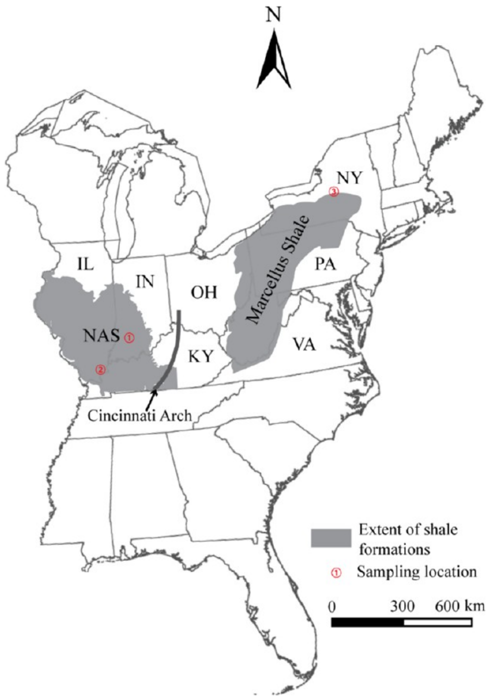

Figure 1. Map showing the locations of sampling sites and the extent of the NAS (Illinois Basin) and Marcellus Shale (Appalachian Basin). NAS = New Albany Shale. ①—NAS from Daviess County, Indiana; ②—NAS from Hicks Dome, Illinois; and ③—Marcellus Shale from Canastota, New York.

samples were measured using a Zeiss Photoscope III microscope; more than 25 readings were taken on each sample. Vitrinite and SB were distinguished based on the dispersed particle occurrence of vitrinite and void-filling and embayment texture of SB.[37] Organic petrographic characteristics of macerals in shale samples were documented using a reflected-light microscope (Leica DM2500 P) in reflected white light and oil immersion as well as under blue light.

2.2.2. TOC Content. The TOC contents of shale samples were measured using a LECO elemental analyzer (SC832DR). During the TOC measurements, 1.50 g of powdered samples were treated with 10 wt % HCl to remove carbonate minerals, followed by washing with distilled water. Solid residues after acid treatment were freeze-dried and combusted in the LECO elemental analyzer. The amounts of generated CO_2 were converted to the organic C content in solid residues and then recalculated to TOC contents of the corresponding shale samples.

2.2.3. X-ray Powder Diffraction. X-ray diffraction (XRD) analysis was conducted on shale samples to study their mineralogical compositions. XRD patterns were acquired with a Bruker D8 Advance X-ray diffractometer using CuKα radiation (45 kV, 35 mA) and a Sol-X solid-state detector. Powdered samples were scanned from 2 to 70° 2θ with a step size of 0.02° and a count time of 2 s. Quantitative Rietveld analysis[43] of the shale samples was performed using TOPAS V5 (Bruker AXS) software. The XRD data of kaolinite and quartz silt are shown in Table S1.

2.2.4. SEM Imaging. The shale composition and pores were imaged on argon ion-milled surfaces with a field-emission SEM (FEI Quanta 400 FEG) in low vacuum mode. Mechanically polished samples were mounted on a custom-designed sample holder and ion milled with a Gatan 600 DuoMill at a low incident angle for 1 to 3 h.[15,23,25] During SEM imaging, the working distance was adjusted to about 10 mm, and the accelerating voltage was 15 kV. A large-field detector was used for detecting secondary electrons in low vacuum mode. The samples were not coated during SEM imaging.

2.2.5. OM Isolation. Shale samples NAS-3, HD-1, and Mar-2 were used for OM isolation for each series of samples (Table 1). 20 g of the powdered samples were treated with 10 wt % HCl for 36 h to remove carbonate minerals. During this time, 10 wt % HCl was added intermittently and solutions were stirred to ensure the complete reaction of carbonate minerals with HCl. When all carbonate minerals were dissolved, the clear supernatant was siphoned out of the beaker. A stoichiometrically excessive volume of cold 24 wt % HF was then added to remove silicate minerals (mostly quartz, feldspars, and clay minerals). After acid treatment, solid residues were rinsed with distilled water to remove excess acid. Isolated OM was recovered with an aspirator on Fisherbrand filter papers (P5 Grade). Pyrite removal from isolated OM was not conducted because current depyritization methods have proven to be inefficient[44] and pyrite shows no significant adsorption in low-pressure N_2 and CO_2 adsorption isotherms.[31] The sulfur content in isolated OM was measured using the same LECO elemental analyzer (SC832DR) as for TOC analysis

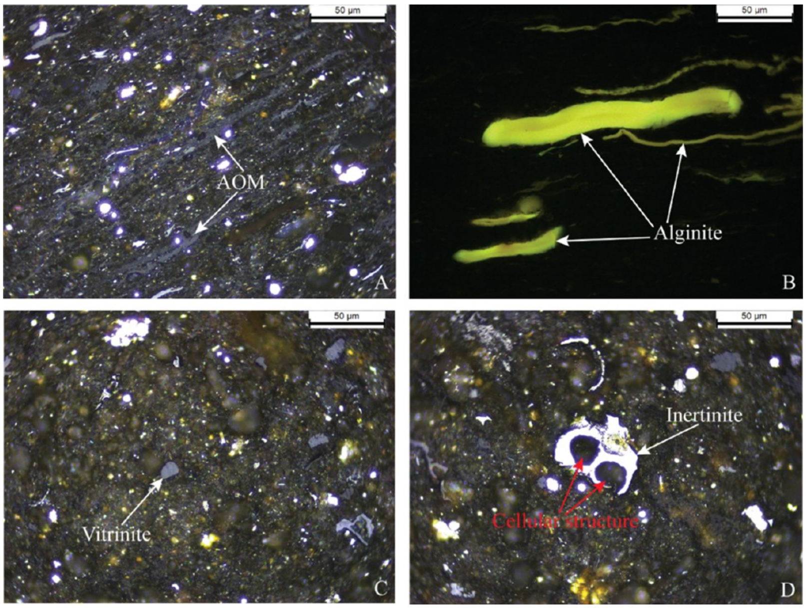

Figure 2. Photomicrographs of OM in the marginally mature NAS samples (R_o 0.55%) in reflected white light and oil immersion (A, C, D) and in fluorescence mode (B). Inertinite in panel D shows a cellular structure filled with diagenetic quartz. AOM = amorphous OM.

https://doi.org/10.1021/acs.energyfuels.1c00526
Energy Fuels XXXX, XXX, XXX−XXX

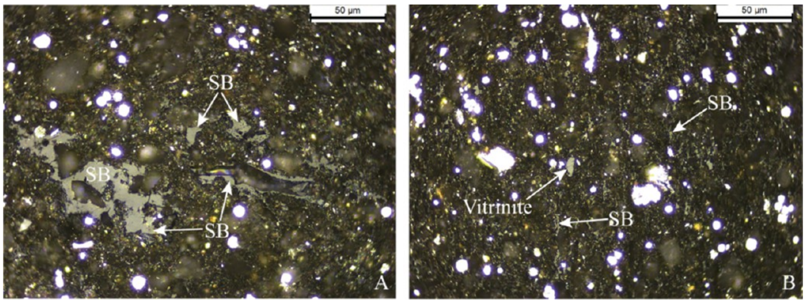

Figure 3. Photomicrographs of OM in the NAS samples in the condensate-wet gas window (R_o 1.05%) in reflected white light and oil immersion. SB = solid bitumen.

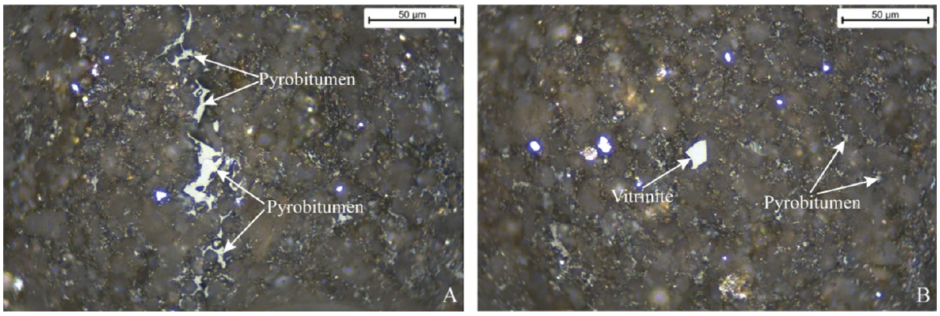

Figure 4. Photomicrographs of OM in the dry gas-window-maturity Marcellus Shale samples (R_o 2.41%) in reflected white light and oil immersion.

and was used to calculate the pyrite content in isolated OM, which was used to calculate the pore structure characteristics of pyrite-free OM based on mass balance. Because bitumen is a natural fraction of OM and influences the pore structure of bulk shales,[10,45] bitumen extraction was not conducted.

2.2.6. Low-Pressure N_2 and CO_2 Adsorption. Pores in shales are classified into micropores (pore diameter < 2 nm), mesopores (2−50 nm diameter), and macropores (pore diameter > 50 nm).[46] Shale samples were crushed and ground to pass 200 mesh (75 μm), which has been shown to be the optimal particle size for performing low-pressure N_2 and CO_2 adsorption analyses on shales.[47] Low-pressure N_2 and CO_2 adsorption measurements of shale samples, kaolinite, quartz silt, and isolated OM were performed using a Micromeritics ASAP-2020 porosimeter and surface area analyzer. Prior to adsorption analysis, the samples were degassed under vacuum at 110 °C for 16 h to remove the adsorbed moisture and volatile matter.

For N_2 adsorption, adsorption isotherms were acquired at the liquid nitrogen temperature (77.35 K at 101.3 kPa), with a relative pressure (p/p_0; p_0 is the saturation vapor pressure of the adsorbed gas) ranging from 0 to 0.99. Both adsorption and desorption analyses were conducted, and only the adsorption branch was used to determine the specific surface area (SSA) and mesopore characteristics. Brunauer−Emmett−Teller (BET) theory was used to calculate the SSA.[48,49] Barrett−Joyner−Halenda (BJH) theory was used to obtain the mesopore pore volume, mesopore size, and mesopore size distribution.[49−51]

For CO_2 adsorption, the temperature at which adsorption occurred was 0 °C (273.15 K), and relative pressure (p/p_0) ranges from 0 to 0.03. The micropore SSA was obtained using the Dubinin−Radushkevich (D−R) equation.[49] The micropore volume and micropore size were obtained with the Dubinin−Astakhov (D−A) equation.[49]

For both N_2 and CO_2 adsorptions, the equilibrium interval was set at 30 s and the relative pressure tolerance was set at 5%. The repeatability of the analysis for the instrumentation is ±3%.

3. RESULTS

3.1. Shale Composition.

3.1.1. OM Composition. The R_o values of NAS samples from Indiana and Illinois are 0.55% and 1.05%, suggesting marginal and early condensate-wet gas-window maturities, respectively. Marcellus shale samples have an R_o of 2.41%, suggesting dry gas-window maturity.

The TOC contents of six marginally mature NAS samples, four condensate-wet gas-window-maturity NAS samples, and four dry gas-window-maturity Marcellus Shale samples range from 4.75 to 12.88 wt % (average 8.94 wt %), 3.47−7.12 wt % (average 5.19 wt %), and 1.64−13.65 wt % (average 6.77 wt %), respectively (Table 1).

When examined under a microscope in reflected light, OM in the marginally mature NAS samples is composed of primary macerals, including amorphous organic matter (AOM), alginite, liptodetrinite, vitrinite, and inertinite (Figure 2), which are common primary macerals in marginally and early mature Devonian marine black shales in the eastern United States.[9,18,35,37,41,54−57] Marine OM, including AOM and alginite, dominates the OM composition at this maturity, whereas terrestrial OM, including vitrinite and inertinite, is typically <10 vol % of total OM and occurs as dispersed particles in the mineral matrix.[9,37,41,55,56]

OM in the NAS samples in the condensate-wet gas window is dominated by SB with minor amounts of vitrinite and inertinite (Figure 3). Primary oil-prone macerals, such as AOM, alginite, and liptodetrinite, have transformed into hydrocarbons and SB and can no longer be identified as distinct components under a microscope.[37] SB occupies the interparticle space between mineral grains and occurs as fine void-filling wisps (Figure 3).

As with the condensate-wet gas-window-maturity NAS samples, the dry gas-window-maturity Marcellus Shale samples have lost their primary oil-prone macerals, and their OM is dominated by pyrobitumen (Figure 4). The thermal maturity boundary value between SB and pyrobitumen is SB reflectance 1.50% for typical non-sulfur-rich kerogen according to Mastalerz et al.[36] The appearance of pyrobitumen in the dry

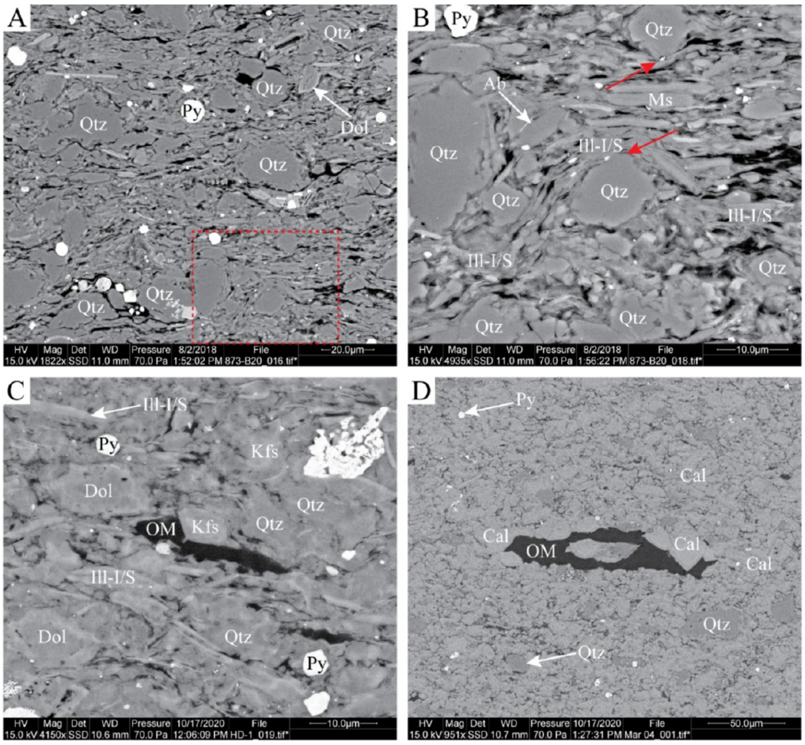

Figure 5. SEM images (backscattered electron mode) showing shale mineralogy. (A,B) Marginally mature NAS (R_o 0.55%). Panel B is the close-up view of the red dashed framed area in panel A. Note the differential compaction of clay minerals against rigid quartz grains (red arrows) in panel B. Sample NAS-5. (C) NAS in the condensate-wet gas window (R_o 1.05%). Sample HD-1. (D) Dry gas-window-maturity Marcellus Shale (R_o 2.41%). Sample Mar-4. Qtz = quartz; Kfs = K-feldspar; Ab = albite; Ill−I/S = illite−illite/smectite; Dol = dolomite; Py = pyrite; Ms = muscovite; OM = organic matter. Minerals were identified based on EDS analysis.

Table 2. Vitrinite Reflectance (R_o), TOC Content, and Pore Structure Characteristics of Shales, Isolated OM, Kaolinite, and Quartz Silt Determined by Low-Pressure N_2 and CO_2 Adsorption[a]

			N_2 adsorption		CO_2 adsorption	
sample	R_o (%)	TOC (wt %)	BET SSA (m^2/g)	BJH mesopore volume (cm^3/g)	D−R micropore surface area (m^2/g)	D−A micropore volume (cm^3/g)
NAS-1	0.55	12.88	8.27	0.0270	25.50	0.0176
NAS-2	0.55	10.05	7.66	0.0238	21.09	0.0157
NAS-3	0.55	12.53	7.61	0.0241	25.43	0.0180
NAS-4	0.55	6.06	7.39	0.0250	10.80	0.0111
NAS-5	0.55	4.75	8.91	0.0285	11.91	0.0123
NAS-6	0.55	7.37	8.33	0.0250	14.24	0.0122
NAS-OM	0.55	50.34	20.89	0.0759	63.68	0.0481
HD-1	1.05	6.52	6.63	0.0215	28.69	0.0181
HD-3	1.05	3.64	6.12	0.0169	9.17	0.0069
HD-5	1.05	7.12	7.42	0.0233	16.98	0.0096
HD-7	1.05	3.47	3.75	0.0116	7.91	0.0049
HD-OM	1.05	36.09	27.23	0.0808	54.23	0.0326
Mar-1	2.41	1.64	6.28	0.0180	6.43	0.0056
Mar-2	2.41	13.65	53.99	0.0374	49.88	0.0241
Mar-3	2.41	8.36	29.45	0.0248	28.77	0.0131
Mar-4	2.41	3.44	15.70	0.0221	14.51	0.0091
Mar-OM	2.41	55.15	65.51	0.0691	86.17	0.0452
kaolinite	n.a.	n.a.	14.88	0.0512	7.37	0.0071
quartz silt	n.a.	n.a.	1.71	0.0049	1.28	0.0048

[a] NAS-OM, HD-OM, and Mar-OM are isolated OM from marginally mature NAS samples (R_o 0.55%), condensate-wet gas-window-maturity NAS samples (R_o 1.05%), and dry gas-window-maturity Marcellus Shale samples (R_o 2.41%), respectively. BET = Brunauer−Emmett−Teller; BJH = Barrett−Joyner−Halenda; D−R = Dubinin−Radushkevich; D−A = Dubinin−Astakhov; and SSA = specific surface area. n.a. = not applicable.

gas window (Figure 4) is similar to that of SB in the condensate-wet gas window (Figure 3).

3.1.2. Mineralogical Composition. XRD analysis shows that the NAS samples consist of quartz, feldspars, clay minerals, dolomite, pyrite, marcasite, and gypsum (Table 1;

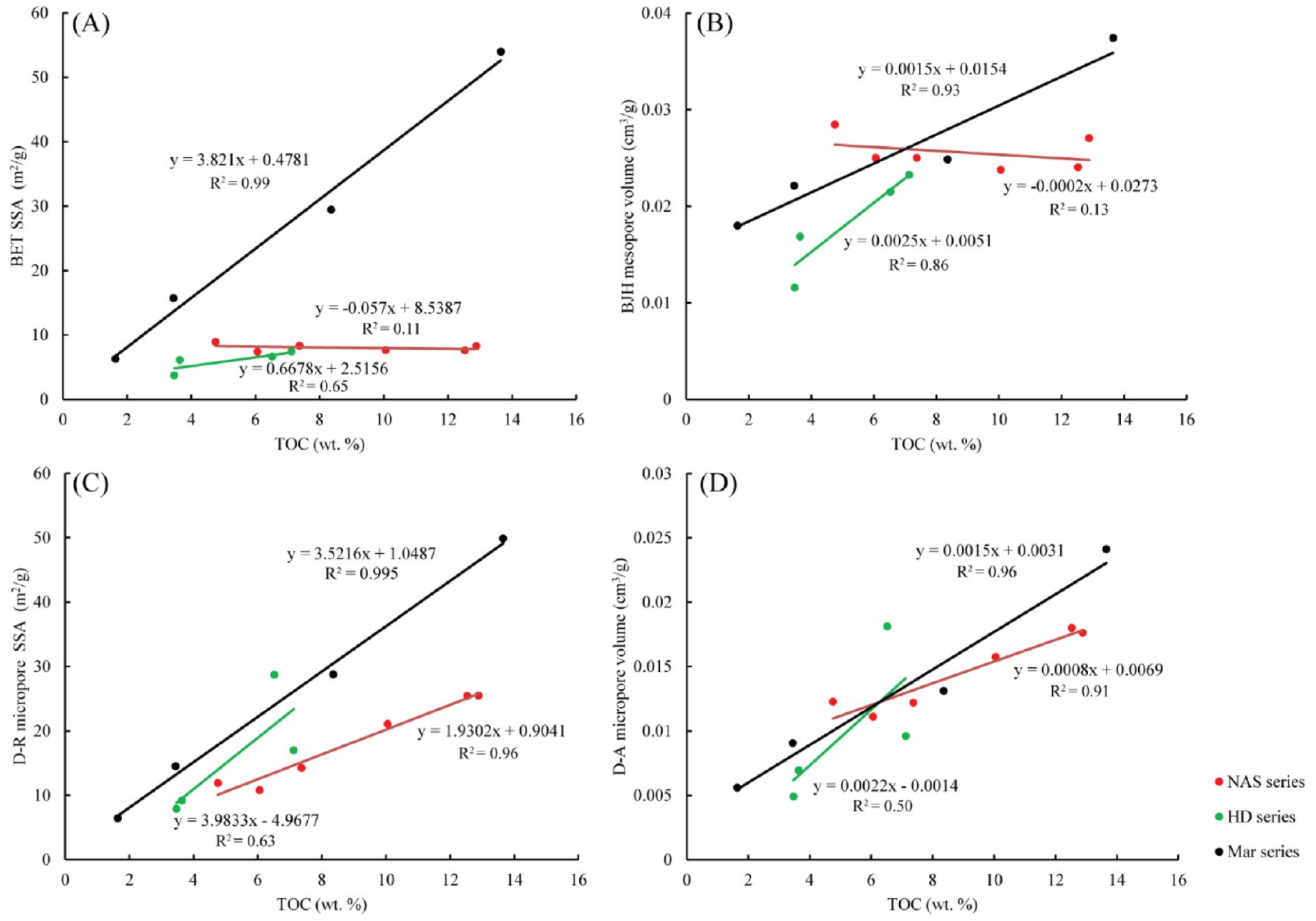

Figure 6. Relationships between the TOC content and (A) BET SSA; (B) BJH mesopore volume; (C) D−R micropore surface area; and (D) D−A micropore volume. NAS series—marginally mature NAS (R_o 0.55%); HD series—NAS in the condensate-wet gas window (R_o 1.05%); and Mar series—Marcellus Shale in the dry gas window (R_o 2.41%).

Figure 5A−C). In terms of weight %, the marginally mature NAS samples contain 36% quartz, 13% feldspars, 45% clay minerals, 2.6% pyrite, 2% dolomite, and 1.3% marcasite on average, with trace amounts of gypsum. In comparison, NAS samples in the condensate-wet gas window contain more quartz and less clay minerals, with 57% quartz, 13% feldspars, 20% clay minerals, 5% dolomite, 4.4% pyrite, and 1.3% marcasite on average (Table 1). Feldspars in both series of samples include orthoclase, microcline, and albite. Clay minerals in the marginally mature NAS samples are dominated by illite, with minor amounts of chlorite and kaolinite. Illite is present as interstratified illite/smectite with 10−20% expandable layers,[58] and no discrete smectite was detected by XRD. In comparison, in the condensate-wet gas-window-maturity NAS samples, the clay minerals consist of only interstratified illite/smectite, with no chlorite or kaolinite. Clay minerals are ductile components compared with quartz, feldspar, and pyrite, as suggested by the differential compaction of clay mineral platelets against rigid grains (Figure 5A,B).

The mineralogy of the dry gas-window-maturity Marcellus Shale samples is dominated by calcite (average 58%), with the exception of sample Mar-2 (16% calcite) (Table 1). Quartz, feldspar, and clay minerals account for 20%, 4%, and 15% of the shale mineral composition on average, respectively (Table 1).

3.2. Low-Pressure N_2 and CO_2 Adsorption.

3.2.1. Shale Samples. As determined by low-pressure N_2 adsorption, the BET SSA of marginally mature NAS samples ranges from 7.39 to 8.91 m^2/g, with an average value of 8.03 m^2/g, and the BJH mesopore volume ranges from 0.0238 to 0.0285 cm^3/g, with an average value of 0.0255 cm^3/g (Table 2). The BET SSA and BJH mesopore volumes of shale samples have no relationships (R^2 = 0.11 and 0.13) with the TOC content (Figure 6A,B) but are positively correlated (R^2 = 0.69 and 0.83) with the clay mineral content (Figure 7A,B), which indicates that the SSA and mesopores in marginally mature shales are mainly contributed by clay minerals.

CO_2 adsorption results show that the D−R micropore surface area of the marginally mature NAS samples ranges from 10.80 to 25.50 m^2/g, and the D−A micropore volume ranges from 0.0111 to 0.0180 cm^3/g (Table 2). The micropore surface area and volume are strongly positively correlated (R^2 = 0.96 and 0.91) with the TOC content (Figure 6C,D) but are slightly negatively correlated (R^2 = 0.37 and 0.25) with the clay mineral content (Figure 7C,D), indicating that micropores in shale mainly occur in OM at marginal maturity.

The BET SSA and BJH mesopore volumes of the condensate-wet gas-window-maturity NAS samples range from 3.75 to 7.42 m^2/g (average 5.98 m^2/g) and 0.0116 to 0.0233 cm^3/g (average 0.0183 cm^3/g), respectively (Table 2). Positive correlations exist between the BET SSA and BJH

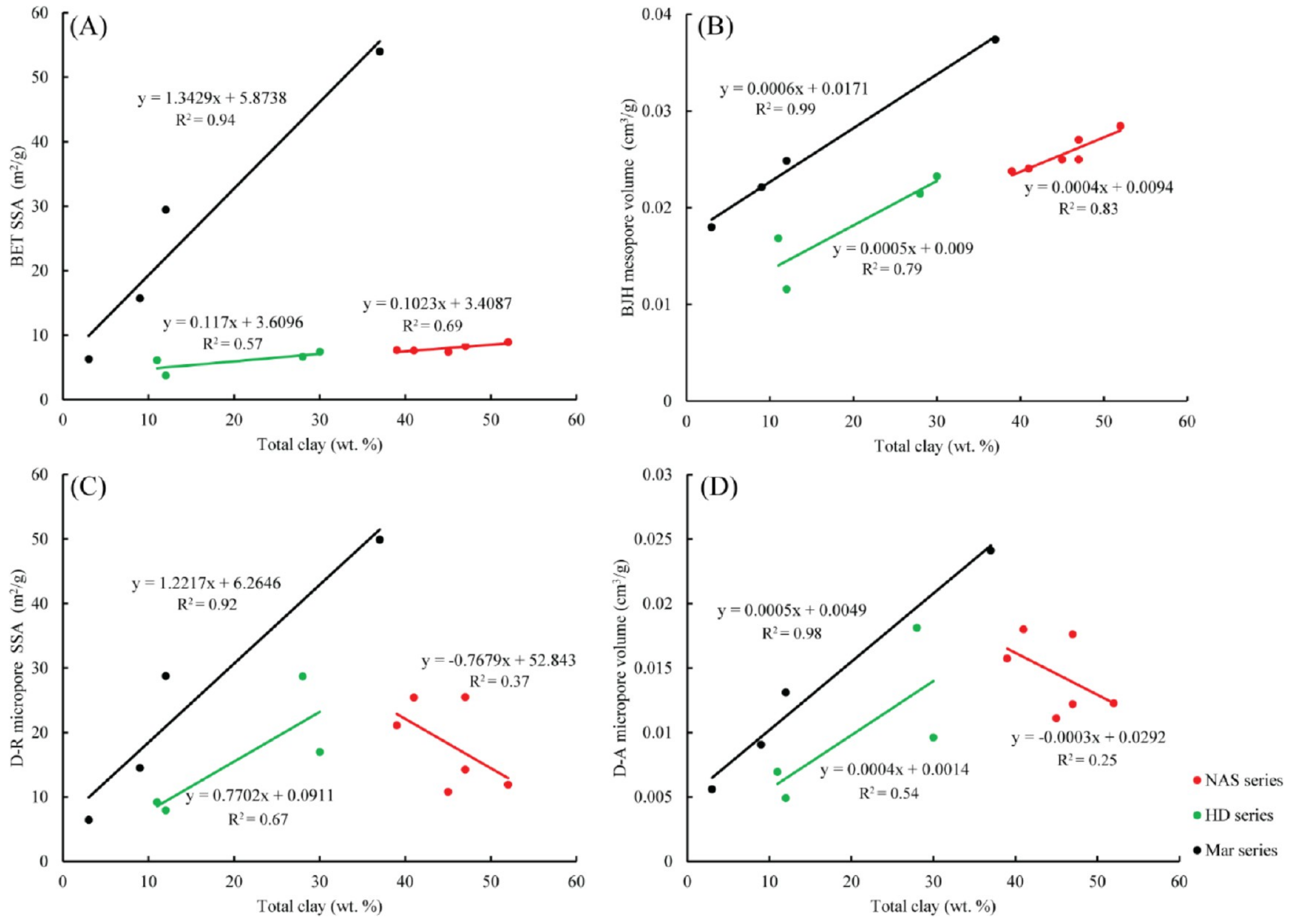

Figure 7. Relationships between (A) BET SSA; (B) BJH mesopore volume; (C) D–R micropore surface area; and (D) D–A micropore volume and total clay mineral contents. NAS series—marginally mature NAS (R_o 0.55%); HD series—NAS in the condensate-wet gas window (R_o 1.05%); and Mar series—Marcellus Shale in the dry gas window (R_o 2.41%).

Table 3. Calibration of Pore Structure Characteristics of Pure OM Based on TOC Content of Isolated OM[a]

	measured values									corrected values			
Sample	BET SSA (m^2/g)	BJH mesopore volume (cm^3/g)	D–R micropore surface area (m^2/g)	D–A micropore volume (cm^3/g)	TOC (wt %)	TS (wt %)	pyrite (wt %)	OM (wt %)	OM + pyrite (wt %)	BET SSA (m^2/g)	BJH mesopore volume (cm^3/g)	D–R micropore surface area (m^2/g)	D–A micropore volume (cm^3/g)
NAS-OM	20.89	0.0759	63.68	0.0481	50.34	18.10	33.94	65.89	99.83	31.70	0.1152	96.65	0.0731
HD-OM	27.23	0.0808	54.23	0.0326	36.09	19.80	37.13	43.48	80.60	62.64	0.1857	124.73	0.0749
Mar-OM	65.51	0.0691	86.17	0.0452	55.15	21.75	40.78	61.27	102.05	106.92	0.1129	140.64	0.0738

[a] NAS-OM, HD-OM, and Mar-OM represent isolated OM from marginally mature NAS samples (R_o 0.55%), condensate-wet gas-window-maturity NAS samples (R_o 1.05%), and dry gas-window-maturity Marcellus Shale samples (R_o 2.41%), respectively. TOC contents of pure OM at R_o 0.55, 1.05, and 2.41% are approximately 76.4%, 83%, and 90%, respectively. OM content = (TOC content of isolated OM/TOC content of pure OM) × 100. Corrected values = (measured values/OM content) × 100. Pyrite content is calculated based on the total sulfur (TS) content: pyrite (wt %) = TS (wt %) × 120/64. 120 and 64 are the masses of 1 mol of FeS_2 and 2 mol of S, respectively. Note that the sum of OM and pyrite in samples NAS-OM and Mar-OM is close to 100%, suggesting that these two samples are composed almost completely of OM and pyrite. The sum of OM and pyrite in sample HD-OM is about 80%, suggesting that there are other minerals besides pyrite in this sample, which could be heavy minerals that were not removed during demineralization. BET = Brunauer–Emmett–Teller; BJH = Barrett–Joyner–Halenda; D–R = Dubinin–Radushkevich; D–A = Dubinin–Astakhov; and SSA = specific surface area.

mesopore volumes of shale samples and TOC (R^2 = 0.65 and 0.86; Figure 6A,B) and clay mineral contents (R^2 = 0.57 and 0.79; Figure 7A,B).

The average D–R micropore surface area and D–A micropore volumes of the condensate-wet gas-window-maturity NAS samples are 15.69 m^2/g and 0.0099 cm^3/g, respectively (Table 2). They both positively correlate with TOC (R^2 = 0.63 and 0.50; Figure 6C,D) and clay mineral contents (R^2 = 0.67 and 0.54; Figure 7C,D).

The BET SSA of Marcellus Shale samples ranges from 6.28 to 53.99 m^2/g (average 26.35 m^2/g), and the BJH mesopore volume ranges from 0.0180 to 0.0374 cm^3/g (average 0.0256 cm^3/g; Table 2). The BET SSA and BJH mesopore volumes of shale samples are highly positively correlated with both TOC

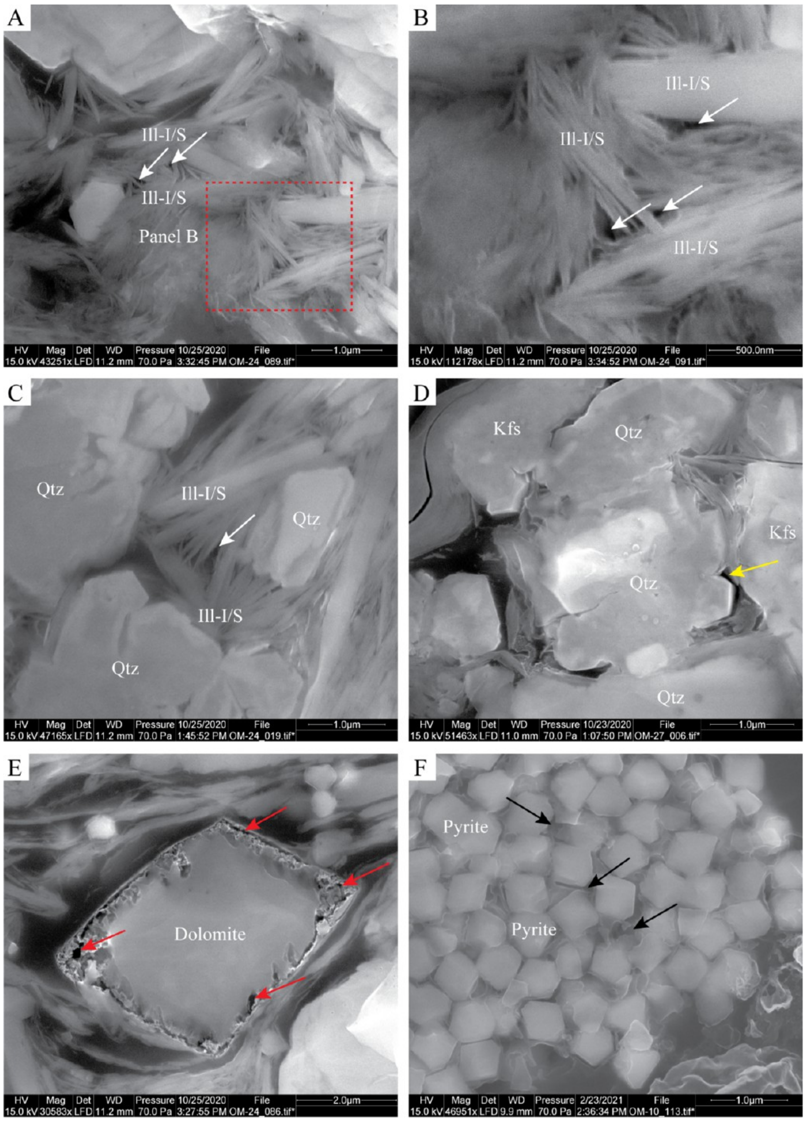

Figure 8. SEM images (secondary electron mode) showing pore types in the marginally mature NAS samples (R_o 0.55%). (A−C) Phyllosilicate framework pores (white arrows) in illite. Panel B is the close-up view of the red dashed area in panel A. Phyllosilicate framework pores are typically triangular. Sample NAS-4. (D) Interparticle pores (yellow arrows) between quartz and K-feldspar. Sample NAS-3. (E) Dolomite dissolution pores (red arrows). Sample NAS-4. (F) Pores within pyrite framboids (black arrows). Sample NAS-6. Ill-I/S = illite−illite/smectite; Qtz = quartz; Kfs = K-feldspar.

(R^2 = 0.99 and 0.93; Figure 6A,B) and clay mineral contents (R^2 = 0.94 and 0.99; Figure 7A,B).

As determined by CO_2 adsorption, the D−R micropore surface area of Marcellus Shale samples ranges from 6.43 to 49.88 m^2/g (average 24.90 m^2/g), and the D−A micropore volume ranges from 0.0056 to 0.0241 cm^3/g (average 0.0130 cm^3/g; Table 2). Similar to the mesopore characteristics, the D−R micropore surface area and D−A micropore volume have strong positive correlations with TOC (R^2 = 0.995 and 0.96; Figure 6C,D) and clay mineral contents (R^2 = 0.92 and 0.98; Figure 7C,D).

3.2.2. OM, Kaolinite, and Quartz Silt. Because OM isolated from shale samples contains varying contents of pyrite that make no significant contribution to adsorption in low-pressure N_2 and CO_2 adsorption isotherms,[31] the pore structure characteristics of pure OM were calibrated based on the OM content of isolated OM, which was calculated based on the TOC content of isolated OM and pure OM at R_o 0.55, 1.05, and 2.41% (76.4, 83, and 90%, respectively).[59,60] The calibrated BET SSA of pure OM at R_o 0.55, 1.05, and 2.41% are 31.70, 62.64, and 106.92 m^2/g, respectively (Table 3).

Kaolinite and quartz silt have BET SSA values of 14.88 and 1.71 m^2/g, respectively (Table 2). Regarding micropore characteristics, the D−R micropore surface areas of kaolinite and quartz silt are 7.37 to 1.28 m^2/g, respectively (Table 2), which are much lower than that of pure OM (Table 3).

Pyrite content is calculated based on the total sulfur (TS) content: pyrite (wt %) = TS (wt %) × 120/64. 120 and 64 are the masses of 1 mol of FeS_2 and 2 mol of S, respectively. Note that the sum of OM and pyrite in samples NAS-OM and Mar-OM is close to 100%, suggesting that these two samples are composed almost completely of OM and pyrite. The sum of OM and pyrite in sample HD-OM is about 80%, suggesting that there are other minerals besides pyrite in this sample, which could be heavy minerals that were not removed during demineralization.

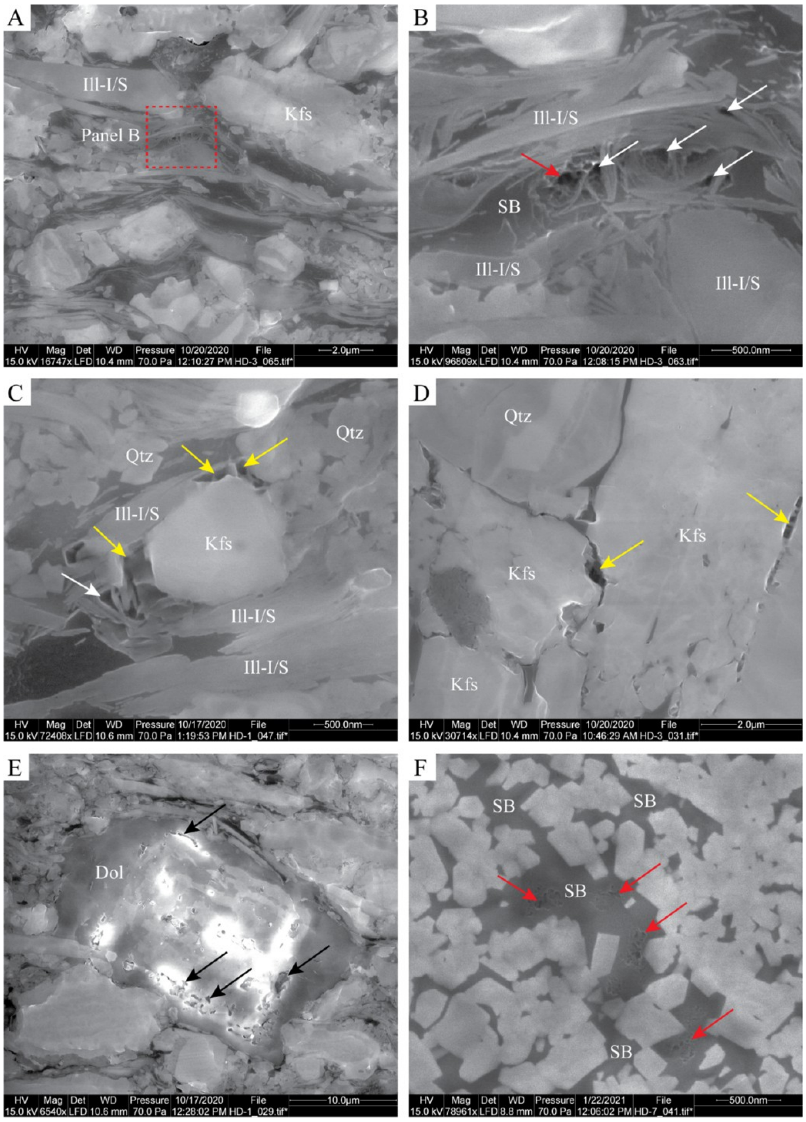

Figure 9. SEM images (secondary electron mode) showing pore types in the NAS samples in the condensate-wet gas window (R_o 1.05%). (A,B) Phyllosilicate framework pores (white arrows) in illite. Panel B is the close-up view of the red dashed area in panel A. Note that SB in image B filled previous phyllosilicate framework pores and developed organic pores (red arrow). Sample HD-3. (C) Interparticle pores (yellow arrows) between K-feldspar and illite. Illite shows triangular phyllosilicate framework pores (white arrow). Sample HD-1. (D) Interparticle pores (yellow arrows) between quartz and K-feldspar. Sample HD-3. (E) Dolomite dissolution pores (black arrows). Sample HD-1. (F) Organic pores (red arrows) hosted by SB. Sample HD-3. Ill−I/S = illite−illite/smectite; Qtz = quartz; Kfs = K-feldspar; Dol = dolomite; SB = solid bitumen.

BET = Brunauer−Emmett−Teller; BJH = Barrett−Joyner−Halenda; D−R = Dubinin−Radushkevich; D−A = Dubinin−Astakhov; and SSA = specific surface area.

3.3. SEM Observations of Pore Types. Pore types in the marginally mature NAS samples include interparticle pores between silt-sized mineral grains (e.g., quartz, feldspar, and clay minerals), phyllosilicate framework pores, and intraparticle pores within mineral grains, such as carbonate dissolution pores and pores in pyrite framboids (Figure 8). No OM-hosted pores were observed under SEM at this maturity.

Similar to the marginally mature NAS samples, mineral matrix-associated pores in the condensate-wet gas-window-maturity NAS samples are dominated by interparticle pores between mineral grains, phyllosilicate framework pores, and dolomite dissolution pores (Figure 9), but they are less common than in the marginally mature NAS samples owing to mechanical compaction, cementation, and pore occlusion via bitumen migration. Organic pores were observed in SB at this maturity (Figure 9F), but they are very rare; the reason for this could be that OM has not generated a substantial amount of gas and/or migrated bitumen and oil filled newly formed organic pores.[37]

Pores in the dry gas-window-maturity Marcellus Shale samples are composed of organic pores, phyllosilicate framework pores, and interparticle pores between calcite crystals and clay platelets, with organic pores being the dominant pore type (Figure 10). Organic pores are hosted by pyrobitumen, and they are more common in the dry gas window than in the condensate-wet gas window. Pyrobitumen-hosted organic pores occur as bubble pores and foam pores (Figure 10D−F).[25] When examined under the SEM, the size of the observed organic pores is typically smaller than 1000 nm and can be as small as 10 nm (Figure 10F).

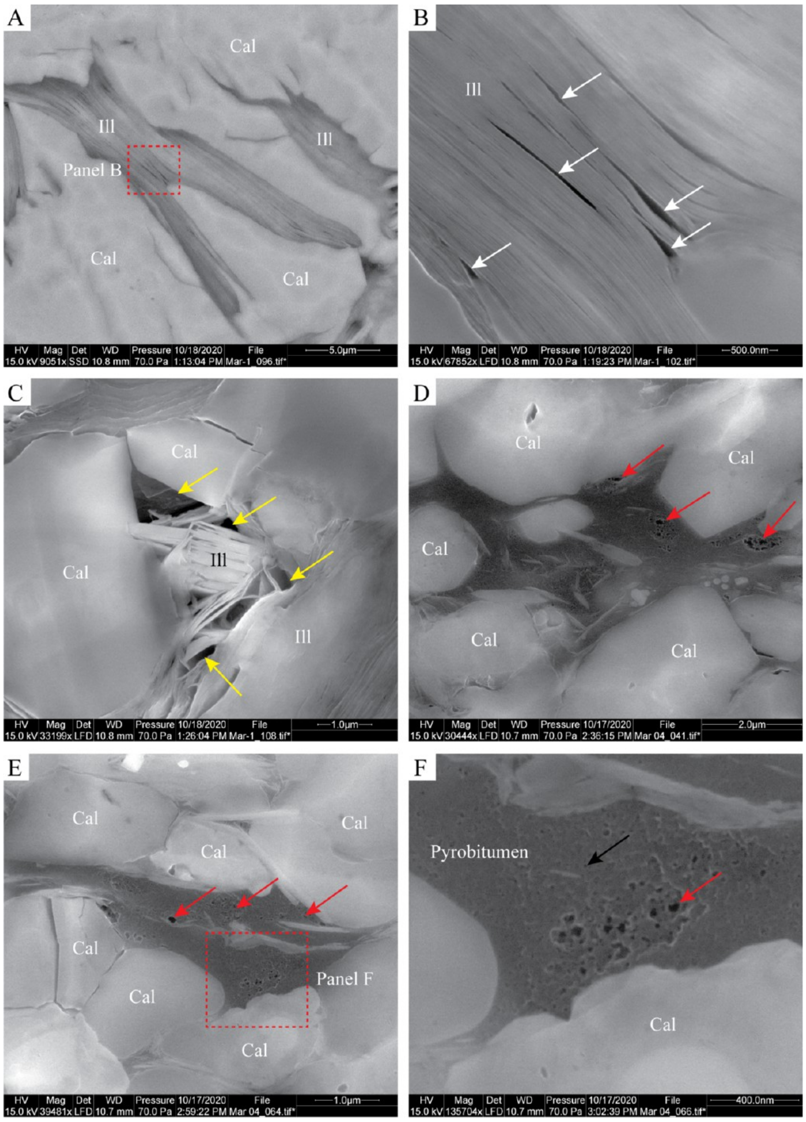

Figure 10. SEM images showing pore types in the dry gas-window-maturity Marcellus Shale samples (R_o 2.41%). Image A is in backscattered electron mode. Images B−F are in secondary electron mode. (A−B) Phyllosilicate framework pores (white arrows) in illite. Panel B is the close-up view of the red dashed area in panel A. Sample Mar-1. (C) Interparticle pores (yellow arrows) between calcite crystals and calcite and illite platelets. Sample Mar-1. (D−F) Organic pores (red arrows) hosted by pyrobitumen. Panel F is the close-up view of the red dashed area in panel E. The smallest pore size (black arrow) on image F is 10 nm. Sample Mar-4. Cal = calcite; Ill = illite.

4. DISCUSSION

4.1. Organic Pore Formation and Preservation.

Organic pores are an important contributor to the pore structure of tight shale reservoirs.[15−19] Organic pores can be primary as well as secondary.[17,18,61] Primary organic pores are pores within structured OM such as inertinite, but they are typically filled with authigenic minerals (e.g., pyrite, early diagenetic silica, or carbonate cement).[18] Secondary organic pores generally develop within secondary OM such as SB and pyrobitumen during thermal maturation of oil-prone OM.[10,14−19,36,61−65] The development of secondary organic pores is controlled by both thermal maturity and OM type.[17,18] Oil-prone primary OM (type I/II kerogen) transforms into hydrocarbons and SB and pyrobitumen during thermal maturation, and secondary organic pores develop within SB or pyrobitumen when oil and gas are generated and expelled.[18,36,61,63] In contrast, gas-prone (type III kerogen) and inert OM (type IV kerogen) do not develop SEM-visible pores with increasing thermal maturity.[18,19,66] In this study, organic pores were observed in SB in the condensate-wet gas-window-maturity NAS samples (Figure 9) and pyrobitumen in the dry gas-window-maturity Marcellus Shale samples (Figure 10) but were not found in primary macerals in the marginally mature NAS samples, indicating that the development of organic pores is significantly impacted by hydrocarbon generation and thermal maturity.

Although no pores were observed in OM under SEM at marginal maturity (R_o 0.55%), gas adsorption analyses show that pure OM at R_o 0.55% has BET SSA and BJH mesopore volume of 31.70 m^2/g and 0.1152 cm^3/g, respectively, and D−R micropore surface area and D−A micropore volume of 96.65 m^2/g and 0.0731 cm^3/g, respectively (Table 3), indicating that OM at marginal maturity contains large amounts of SEM-invisible micropores and mesopores.[9,19,20] Micropores (<2 nm) in OM are interpreted to be pore spaces within the macromolecular structure of OM.[28]

Table 4. Pore Structure Characteristics of Major Minerals in Shales from the Literature and This Study

mineral	BET SSA (m^2/g)	BJH mesopore volume (cm^3/g)	micropore surface area (m^2/g)	micropore volume (cm^3/g)
smectite	24.7; 31.13; 29.8; 31.82−97.42; 75.9; 71.5; 56.5	0.068	28.3	0.0078
illite	30; 31.57; 30.5; 67.2; 31.31; 11.2; 11.38; 24.3	0.03; 0.033; 0.037	29.4; 20.7	0.0079; 0.007
kaolinite	7.1; 11.49; 20.2; 6.6−10.05; 21; 12.41; 15.7; 11.93; 7.8; 14.88[a]	0.049; 0.0734; 0.033; 0.0512[a]	9.8; 5.4; 7.37[a]	0.0027; 0.002; 0.0071[a]
chlorite	2.1; <1; 4.4; 5.32	0.0249	4.8	0.0013
quartz	0.35; 1.7; 1.71[a]	0.0049[a]	3.12; 1.28[a]	0.0008; 0.0048[a]
pyrite	0.2−4			

[a] This study. SSA = specific surface area.

The BET SSA of isolated OM from the studied shales increases from 31.70 m^2/g at R_o 0.55% to 62.64 m^2/g at R_o 1.05% and 106.92 m^2/g at R_o 2.41% (Table 3), which further supports the control of thermal maturity on the organic pore development. The evolution of the BET SSA of isolated OM with increasing thermal maturity in this study is consistent with the previous studies of the evolution of BET SSA of isolated OM from black shales of varying ages and thermal maturities.[18,67] Interestingly, the mesopore and micropore volumes of OM do not show significant changes with increasing maturity (Table 3), which is likely because the rearrangement of the macromolecular structure of OM did not result in a significant loss of the pore volume but caused an increase in SSA through reducing the pore size.

4.2. Mineral Matrix-Associated Pores. Mineral matrix-related pores contribute significantly to the pore system of tight shale reservoirs because organic-lean shales still possess appreciable porosity.[68] Interparticle pores between mineral grains are often associated with compaction-resistant grains, and their preservation is primarily controlled by compaction and cementation during diagenesis.[15,16,68] Intraparticle pores within mineral grains commonly occur as dissolution pores in carbonate minerals and as pores in pyrite framboids.[15,16] Carbonate dissolution pores are generally secondary in origin and their development is likely linked to organic acid formation during the transformation of OM.[15,69] In this study, interparticle pores exist in all samples but become less common with increasing thermal maturity, which is likely due to higher burial pressure, cementation, and pore occlusion by bitumen.

Mineralogical composition critically controls the petrophysical properties of shales.[2,70] Clay minerals host phyllosilicate framework pores and contribute significantly to the SSA and micropore volumes of shales,[7,8,11] with smectite and illite having higher SSA and micropore volumes than kaolinite and chlorite (Table 4).[7,8,10,71−77] Silt-sized grains, such as quartz, feldspar, calcite, and pyrite, have very low SSA and micropore volumes (Table 4)[7,72,74] but can host interparticle pores and contribute to the total porosity. The measured pore structure characteristics of the kaolinite and quartz silt in this study are comparable to those reported in prior studies (Table 4).[7,8,10,71,73−77]

OM has a BET SSA of 31.70 m^2/g at R_o 0.55% (Table 3), which is close to that of typical illite (~30 m^2/g; Table 4). Because the clay mineral content is much higher than the TOC content in marginally mature NAS samples and in most black shales in general; clay minerals contribute more SSA to bulk shales than OM at marginal and early maturity. The BET SSA of OM reaches 106.92 m^2/g at R_o 2.41% (Table 3), which is approximately 3.5 times that of illite. However, if the clay mineral (mostly illite at this maturity) content in a shale sample is more than 3.5 times OM content, the SSA of bulk shales will be dominated by clay minerals, although OM has a much higher SSA than clay minerals per unit mass. This reasoning also applies to the BJH mesopore volumes, D−R micropore surface area, and D−A micropore volumes of shales. Therefore, the pore structure characteristics of bulk shales depend on the clay mineral content and type, as well as by the OM content and thermal maturity.

4.3. Compositional Control on the Shale Pore Structure. The pore structure characteristics of shales are fundamentally controlled by the shale composition, especially the abundance of OM and clay minerals.[7−12] Therefore, the BET SSA, BJH mesopore volumes, D−R micropore surface area, and D−A micropore volumes of shales can be estimated by summing the contents (weight percent %) of individual components multiplied by their corresponding properties using eqs 1−4.

$$\begin{aligned}\mathrm{BET_{shale}} = {} & \mathrm{BET_{OM}} \times \mathrm{TOC} + [30 \times W_{\mathrm{illite}} \\ & + 14.88 \times W_{\mathrm{kaolinite}} + 2.1 \times W_{\mathrm{chlorite}} \\ & + 1.71 \times (1 - W_{\mathrm{clay}})] \times (1 - \mathrm{TOC})\end{aligned} \tag{1}$$

$$\begin{aligned}\mathrm{BJH_{shale}} = {} & \mathrm{BJH_{OM}} \times \mathrm{TOC} + [0.03 \times W_{\mathrm{illite}} \\ & + 0.0512 \times W_{\mathrm{kaolinite}} + 0.0512 \times W_{\mathrm{chlorite}} \\ & + 0.0049 \times (1 - W_{\mathrm{clay}})] \times (1 - \mathrm{TOC})\end{aligned} \tag{2}$$

$$\begin{aligned}\mathrm{D{-}R_{shale}} = {} & \mathrm{D{-}R_{OM}} \times \mathrm{TOC} + [29.4 \times W_{\mathrm{illite}} \\ & + 7.37 \times W_{\mathrm{kaolinite}} + 4.8 \times W_{\mathrm{chlorite}} \\ & + 1.28 \times (1 - W_{\mathrm{clay}})] \times (1 - \mathrm{TOC})\end{aligned} \tag{3}$$

$$\begin{aligned}\mathrm{D{-}A_{shale}} = {} & \mathrm{D{-}A_{OM}} \times \mathrm{TOC} + [0.0079 \times W_{\mathrm{illite}} \\ & + 0.0071 \times W_{\mathrm{kaolinite}} + 0.0013 \times W_{\mathrm{chlorite}} \\ & + 0.0048 \times (1 - W_{\mathrm{clay}})] \times (1 - \mathrm{TOC})\end{aligned} \tag{4}$$

where $\mathrm{BET_{shale}}$ and $\mathrm{BET_{OM}}$ are the BET SSA (m^2/g) of the bulk shale and corresponding OM, respectively. $\mathrm{BJH_{shale}}$ and $\mathrm{BJH_{OM}}$ are the BJH mesopore volumes (cm^3/g) of the bulk shale and corresponding OM, respectively. $\mathrm{D{-}R_{shale}}$ and $\mathrm{D{-}R_{OM}}$ are the D−R micropore surface areas (m^2/g) of the bulk shale and corresponding OM, respectively. $\mathrm{D{-}A_{shale}}$ and $\mathrm{D{-}A_{OM}}$ are the D−A micropore volumes (cm^3/g) of the bulk shale and corresponding OM, respectively. The TOC content is represented by TOC (wt %). W_{illite}, $W_{\mathrm{kaolinite}}$, W_{chlorite}, and W_{clay} are the contents (wt %) of illite, kaolinite, chlorite, and total clay, respectively.

https://doi.org/10.1021/acs.energyfuels.1c00526

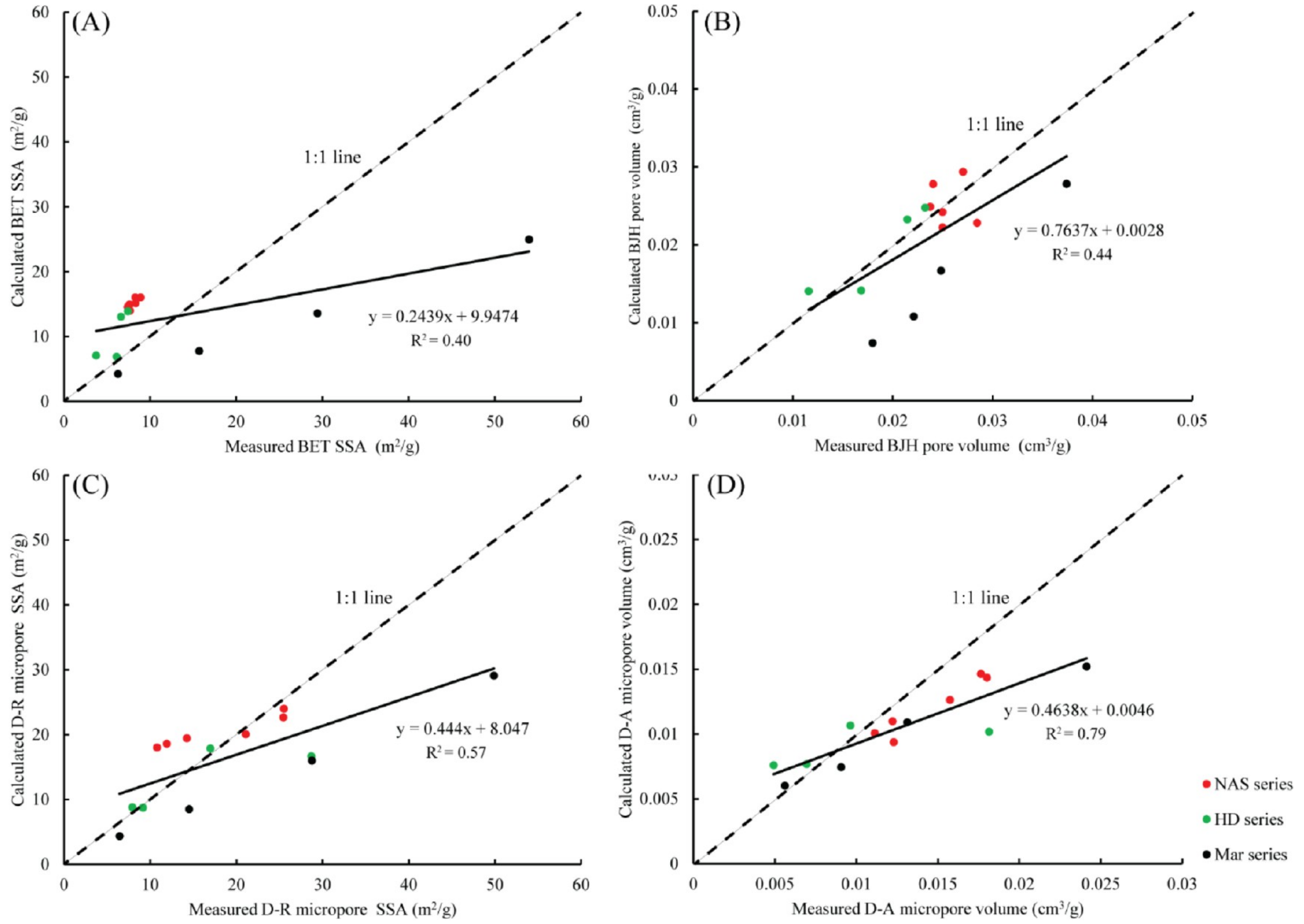

Figure 11. Relationships between the calculated and measured (A) BET SSA; (B) BJH mesopore volume; (C) D−R micropore surface area; and (D) D−A micropore volume. The calculated pore characteristics of shales are based on the calibrated values of OM listed in Table 3. NAS series—marginally mature NAS (R_o 0.55%); HD series—NAS in the condensate-wet gas window (R_o 1.05%); Mar series—Marcellus Shale in the dry gas window (R_o 2.41%). The 1:1 line indicates where the calculated values equate the measured values. SSA = specific surface area.

The BET_{OM}, BJH_{OM}, $D-R_{OM}$, and $D-A_{OM}$ vary with thermal maturity. Calibrated values listed in Table 3 are used. The BET SSA (30 and 2.1 m^2/g), D−R micropore surface area (29.4 and 4.8 m^2/g), and D−A micropore volumes (0.0079 and 0.0013 cm^3/g) of illite and chlorite are from Ross and Bustin.[7] These values were obtained on illite (IMt-2) and chlorite (CCa-2) standards. The BET SSA of illite (30 m^2/g) is close to that of shales (31.57 m^2/g[8]) dominated by illite (89 wt %) interstratified with illite/smectite, which is similar to the nature of illite in this study. Because micropore characteristics of illite are also available in Ross and Bustin,[7] the values of illite from Ross and Bustin[7] are used in the calculations. The BJH mesopore volume of illite (0.03 cm^3/g) is from Kuila and Prasad.[8] The BJH mesopore volume of chlorite (0.0249 cm^3/g) is from Wang et al.[76] The BET SSA, BJH mesopore volumes, D−R micropore surface area, and D−A micropore volumes of kaolinite and quartz silt are values reported in this study (Table 2). Because nonclay minerals (e.g., quartz, feldspar, calcite, dolomite, and pyrite) also have low SSA and pore volume, the pore characteristics of non-clay minerals are assumed to be the same as that of quartz silt.

The calculated BET SSA, BJH mesopore volume, D−R micropore surface area, and D−A micropore volume of the NAS samples correlate well with the measured values (Figure 11). The calculated BET SSA values of marginally mature (R_o 0.55%) NAS samples are all higher than the measured values (Figure 11A), the reason for which could be that OM at this maturity has a low BET SSA and the dissociation of OM and minerals during demineralization exposed more surfaces of OM. Thus, the measured values of isolated OM at this maturity are higher than its true values, which results in higher calculated values.

The calculated values all underestimate the mesopore and micropore characteristics of the Marcellus Shale samples (Figure 11), which could be due to the highly microporous nature of OM at this maturity (R_o 2.41%) and inefficient access of pore spaces by adsorptive gases, especially in the N_2 adsorption analysis.[78] Previous studies have shown that the BET equation has limitations in characterizing microporous materials.[78,79] The mesopore and micropore SSAs and pore volumes of the Marcellus Shale samples are highly positively correlated with the TOC content (R^2 = 0.93−0.99; Figure 6). Based on these relationships, the mesopore and micropore volumes and SSAs of OM can be extrapolated assuming a 90% TOC of OM at R_o 2.41%.[60] The extrapolated BET SSA, BJH mesopore volume, D−R micropore surface area, and D−A micropore volume of OM are 344 m^2/g, 0.1504 cm^3/g, 318 m^2/g, and 0.1381 cm^3/g, respectively. The extrapolated SSA of OM is about 2−3 times higher than the measured values (Table 3). The micropore volume also shows an increase from

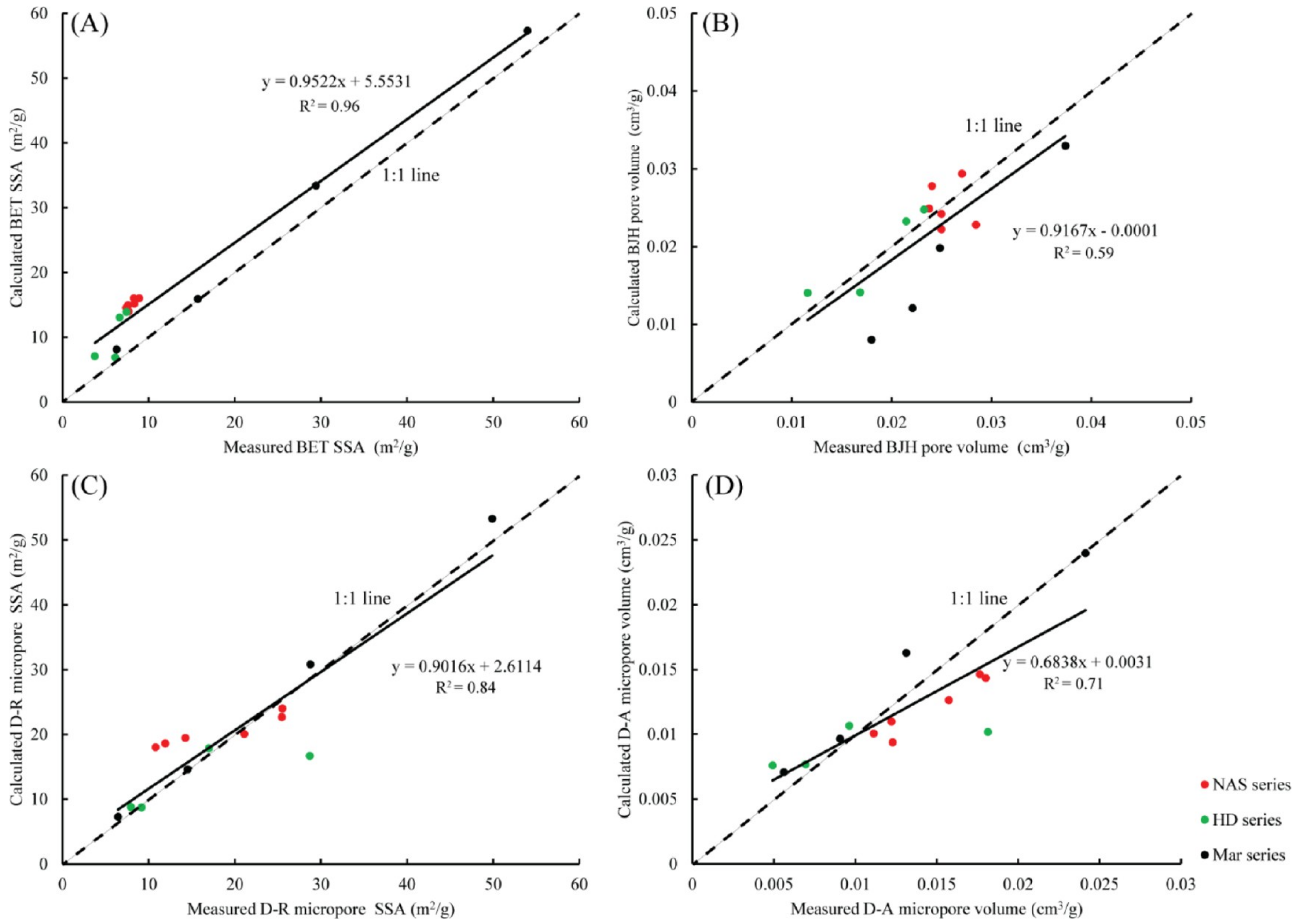

Figure 12. Relationships between the calculated and measured (A) BET SSA; (B) BJH mesopore volume; (C) D−R micropore surface area; and (D) D−A micropore volume. The calculated pore characteristics of Marcellus Shale samples are based on the extrapolated values of OM according to the relationships between pore characteristics and TOC content in Figure 6 and assuming a 90% TOC of OM at R_o 2.41%. The extrapolated BET SSA, BJH mesopore volume, D−R micropore surface area, and D−A micropore volume of OM are 344 m^2/g, 0.1504 cm^3/g, 318 m^2/g, and 0.1381 cm^3/g, respectively. NAS series—marginally mature NAS (R_o 0.55%); HD series—NAS in the condensate-wet gas window (R_o 1.05%); Mar series—Marcellus Shale in the dry gas window (R_o 2.41%). The 1:1 line indicates where the calculated values equate the measured values. SSA = specific surface area.

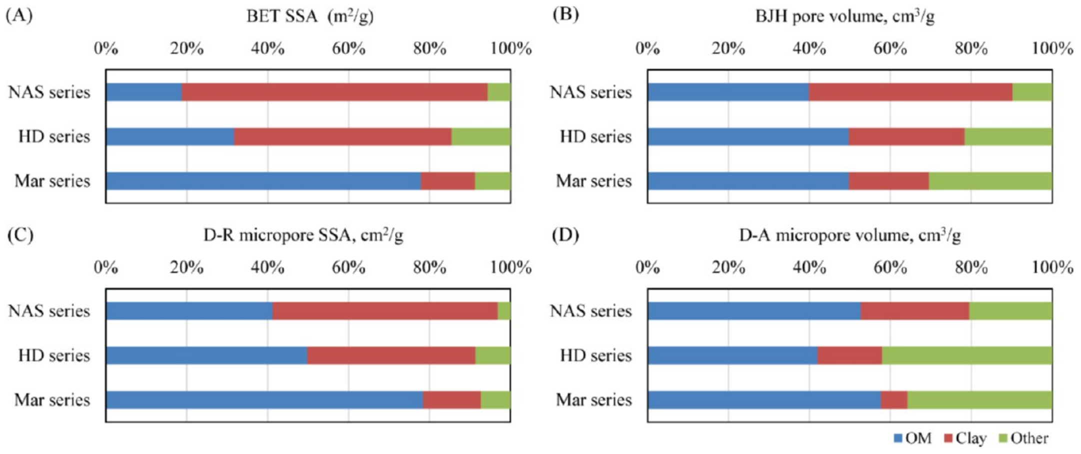

Figure 13. Contribution of OM, clay minerals, and other components to (A) BET SSA; (B) BJH mesopore volume; (C) D−R micropore surface area; and (D) D−A micropore volume of bulk shales. The contribution of OM in the Marcellus Shale samples is based on the extrapolated properties of OM from Figure 6. NAS series—average of the marginally mature NAS samples (R_o 0.55%); HD series—average of the NAS samples in the condensate-wet gas window (R_o 1.05%); and Mar series—average of the Marcellus Shale samples in the dry gas window (R_o 2.41%). SSA = specific surface area. Other components refer to mineral components excluding clay minerals (quartz, feldspar, pyrite, etc.).

R_o 0.55 and 1.05% (Table 3). Employing the extrapolated values of OM in the Marcellus Shale samples, the calculated BET SSA, BJH mesopore volume, D−R micropore surface area, and D−A micropore volume of shales correlate better with the measured values (R^2 = 0.59−0.96), with the best agreement seen for the Marcellus Shale samples (Figure 12). Because the estimated pore structure characteristics of the Marcellus Shale samples using the extrapolated values match better with the measured values than using the measured values of isolated OM (Figures 11, 12), low-pressure N_2 and CO_2 adsorption analyses of OM isolated from black shales may indeed underestimate the pore volume and SSA of OM at high maturity because of the existence of abundant micropores.

Prior studies have attempted to predict the mesopore and micropore volumes and SSAs of shales based on the clay mineral and TOC contents,[12] but clay mineral type and thermal maturity of OM were not considered. The equations derived in this study have broad applications in evaluating the pore structure characteristics of black shales with different thermal maturities and varying clay mineral types. It is important to note, however, that some modifications of these equations (eqs 1−4) might be needed when choosing the pore characteristics of illite, depending on the nature of illite (e.g., the amount of interstratified illite/smectite). For shales that are rich in smectite group minerals, the contribution of smectite group minerals should be added in the calculations. Smectite group minerals have a higher SSA than other clay minerals (Table 4 and references therein).

The mesopore and micropore SSAs and pore volumes of black shales are primarily contributed by OM and clay minerals (Figure 13), with OM making more contributions per unit mass. Because the mesopore and micropore characteristics of the studied Marcellus Shale samples are controlled by OM (Figure 13), the strong positive correlations between the mesopore and micropore SSAs and pore volumes and clay mineral content are caused by the covariation of TOC and clay mineral content (Table 1). Other components (e.g., quartz, feldspar, and pyrite) make only minor contributions except for the micropore volume of the HD series and Mar series samples (Figure 13D) because of the low TOC and clay mineral contents of samples HD-3, HD-7, Mar-1, and Mar-4 (Table 1). When studying the evolution of the pore structure characteristics of shales during thermal maturation, the variations of OM content and clay mineral type and content could mask the evolutionary trend. For example, a high-maturity shale sample (e.g., sample Mar-1 with a BET SSA of 6.28 m^2/g; Table 2) having low TOC and clay mineral contents would have a lower SSA than a low-maturity sample (e.g., sample NAS-1 with a BET SSA of 8.27 m^2/g; Table 2) having high TOC and clay mineral contents. However, it does not indicate that the SSA of shales decrease with thermal maturity. Therefore, to reveal a more realistic evolutionary trend of the pore structure characteristics of shales with increasing maturity, shales having comparable mineralogical compositions but different thermal maturities should be compared. If the loss of OM during the thermal maturation of oil-prone OM is considered, high-maturity shales would have a lower TOC content.

The pore structure properties of shales calculated using eqs 1−4 mostly characterize the mesopore and micropore characteristics of shales that dominate the gas adsorption capacity of shales. The porosity of shales cannot be calculated in the same fashion because it is critically controlled by silt-sized grains and their contact relationships, as well as the diagenetic history of shales. For example, a diagenetic-quartz-rich shale would have a low SSA but a high porosity because quartz has low SSA (Table 4), but diagenetic quartz can form a compaction-resisting fabric that preserves interparticle porosity.[80,81] Diagenetic processes such as compaction and cementation mainly influence the large pores and porosity of shales. Mesopore and micropore properties of shales are primarily controlled by OM maturation and clay mineral transformation.

5. CONCLUSIONS

A combination of SEM imaging and low-pressure N_2 and CO_2 adsorption analyses of black shales of different thermal maturities (R_o 0.55 to 2.41%) from two different basins and major components in shales as well as data from the literature facilitates a quantitative and qualitative characterization of the control of mineralogical and OM compositions on pore structure properties of shales at different stages of hydrocarbon generation.

When examined under SEM, mineral matrix-associated pores are observed in all samples and become less common with increasing maturity. Secondary organic pores do not develop at marginal maturity and increase in abundance from the condensate-wet gas window to the dry gas window.

Low-pressure N_2 and CO_2 adsorption analyses of isolated OM from shales demonstrate that OM at marginal maturity has large amounts of micropores and small mesopores, even though it does not show SEM-visible pores. At marginal maturity, the micropore characteristics of shales are controlled by OM because of the abundance of micropores in the macromolecular structure of OM, but the mesopore characteristics of shales are primarily controlled by clay minerals, depending OM, and clay mineral contents. The mesopore and micropore SSAs of OM increase with increasing maturity and make greater contributions to the pore structure characteristics of bulk shales. The mesopore and micropore characteristics of shales are controlled by OM content and maturity as well as by the clay mineral type and content and can be predicted on the basis of the contents of each component in shales at different stages of thermal maturation.

A correction of the mesopore and micropore properties of isolated OM from shales based on the TOC content is necessary if pyrite and heavy mineral are not completely removed. Low-pressure gas N_2 and CO_2 adsorption analyses of OM isolated from shales with high maturity may underestimate the pore properties of OM because of its highly microporous nature.

■ ASSOCIATED CONTENT

Supporting Information

The Supporting Information is available free of charge at https://pubs.acs.org/doi/10.1021/acs.energyfuels.1c00526.

Mineralogical composition of kaolinite and quartz silt determined by XRD (PDF)

■ AUTHOR INFORMATION

Corresponding Author

Juan Teng − *Indiana Geological and Water Survey, Indiana University, Bloomington, Indiana 47405-2208, United States; College of Energy, Chengdu University of Technology, Chengdu, Sichuan 610059, China;* orcid.org/0000-0003-1171-2612; Email: tengjuancugb@outlook.com

Authors

Bei Liu − *Department of Earth and Atmospheric Sciences, Indiana University, Bloomington, Indiana 47405, United States*

Maria Mastalerz − *Indiana Geological and Water Survey, Indiana University, Bloomington, Indiana 47405-2208, United States*

Juergen Schieber − *Department of Earth and Atmospheric Sciences, Indiana University, Bloomington, Indiana 47405, United States*

Arndt Schimmelmann − *Department of Earth and Atmospheric Sciences, Indiana University, Bloomington, Indiana 47405, United States;* orcid.org/0000-0003-4648-5253

David Bish − *Department of Chemistry, Indiana University, Bloomington, Indiana 47405, United States*

Complete contact information is available at:
https://pubs.acs.org/10.1021/acs.energyfuels.1c00526

Notes

The authors declare no competing financial interest.

ACKNOWLEDGMENTS

This research was supported by the sponsors of the Indiana University Shale Research Consortium (Anadarko, Chevron, ConocoPhillips, ExxonMobil, Shell, Statoil, Marathon, Whiting, Wintershall). An NSF equipment grant to J.S. (EAR-0318769) provided funds for the purchase of the analytical SEM that was used for acquiring the SEM images used in this study. B.L. was also partially supported by the U.S. Department of Energy, Office of Science, Office of Basic Energy Sciences, Chemical Sciences, Geosciences, and Biosciences Division under Award Number DE-SC0006978. Many thanks to editor Dr. John Shaw and four anonymous reviewers for their constructive comments that greatly improved the manuscript.

REFERENCES

(1) Curtis, J. B. Fractured shale-gas systemss. *AAPG Bull.* **2002**, *86*, 1921−1938.

(2) Passey, Q. R.; Bohacs, K. M.; Esch, W. L.; Klimentidis, R.; Sinha, S. From oil-prone source rock to gas-producing shale reservoir-geologic and petrophysical characterization of unconventional shale-gas reservoirs, Chinese Petroleum Society/Society of Petroleum Engineers International Oil and Gas Conference and Exhibition: Beijing, China, June 8−10, 2010; SPE Paper 131350.

(3) Jarvie, D. M. Shale resource systems for oil and gas: Part 1—Shale-gas resource systems. In *Shale Reservoirs—Giant Resources for the 21st Century*; Breyer, J. A., Ed.; American Association of Petroleum Geologists (AAPG); AAPG Memoir: Tulsa, OK, 2012; Vol. 97, pp 69−87.

(4) Jarvie, D. M. Shale resource systems for oil and gas: Part 1—Shale-oil resource systems. In *Shale Reservoirs—Giant Resources for the 21st Century*; Breyer, J. A., Ed.; American Association of Petroleum Geologists (AAPG); AAPG Memoir: Tulsa, OK, 2012; Vol. 97, pp 89−119.

(5) Qiu, Z.; Zou, C. Controlling factors on the formation and distribution of ″sweet-spot areas″ of marine gas shales in South China and a preliminary discussion on unconventional petroleum sedimentology. *J. Asian Earth Sci.* **2020**, *194*, 103989.

(6) Qiu, Z.; Zou, C. Unconventional petroleum sedimentology: Connotation and prospect. *Acta Sedimentol. Sin.* **2020**, *38*, 1−29. (in Chinese with English abstract)

(7) Ross, D. J. K.; Marc Bustin, R. The importance of shale composition and pore structure upon gas storage potential of shale gas reservoirs. *Mar. Pet. Geol.* **2009**, *26*, 916−927.

(8) Kuila, U.; Prasad, M. Specific surface area and pore-size distribution in clays and shales. *Geophys. Prospect.* **2013**, *61*, 341−362.

(9) Mastalerz, M.; Schimmelmann, A.; Drobniak, A.; Chen, Y. Porosity of Devonian and Mississippian New Albany Shale across a maturation gradient: Insights from organic petrology, gas adsorption, and mercury intrusion. *AAPG Bull.* **2013**, *97*, 1621−1643.

(10) Valenza, J. J.; Drenzek, N.; Marques, F.; Pagels, M.; Mastalerz, M. Geochemical controls on shale microstructure. *Geology* **2013**, *41*, 611−614.

(11) Saidian, M.; Godinez, L. J.; Prasad, M. Effect of clay and organic matter on nitrogen adsorption specific surface area and cation exchange capacity in shales (mudrocks). *J. Nat. Gas Sci. Eng.* **2016**, *33*, 1095−1106.

(12) Yuan, Y.; Rezaee, R.; Al-Khdheeawi, E. A.; Hu, S.-Y.; Verrall, M.; Zou, J.; Liu, K. Impact of composition on pore structure properties in shale: Implications for micro-/mesopore volume and surface area prediction. *Energy Fuels* **2019**, *33*, 9619−9628.

(13) Xiong, F.; Rother, G.; Gong, Y.; Moortgat, J. Reexamining supercritical gas adsorption theories in nano-porous shales under geological conditions. *Fuel* **2021**, *287*, 119454.

(14) Teng, J.; Deng, H.; Liu, B.; Chen, W.; Fu, M.; Xia, Y.; Yu, H. Insights of the pore system of lacustrine shales from immature to late mature with the aid of petrology, mineralogy and porosimetry: A case study of the Triassic Yanchang Formation of the Ordos Basin, North China. *J. Pet. Sci. Eng.* **2021**, *196*, 107631.

(15) Schieber, J. Common themes in the formation and preservation of intrinsic porosity in shales and mudstones-illustrated with examples across the Phanerozoic, SPE Unconventional Gas Conference; Society of Petroleum Engineers: Pittsburgh, PA, USA, February 23−25, 2010. SPE Paper 132370.

(16) Loucks, R. G.; Reed, R. M.; Ruppel, S. C.; Hammes, U. Spectrum of pore types and networks in mudrocks and a descriptive classification for matrix-related mudrock pores. *AAPG Bull.* **2012**, *96*, 1071−1098.

(17) Katz, B. J.; Arango, I. Organic porosity: A geochemist's view of the current state of understanding. *Org. Geochem.* **2018**, *123*, 1−16.

(18) Liu, B.; Schieber, J.; Mastalerz, M. Combined SEM and reflected light petrography of organic matter in the New Albany Shale (Devonian-Mississippian) in the Illinois Basin: A perspective on organic pore development with thermal maturation. *Int. J. Coal Geol.* **2017**, *184*, 57−72.

(19) İnan, S.; Al Badairy, H.; İnan, T.; Al Zahrani, A. Formation and occurrence of organic matter-hosted porosity in shales. *Int. J. Coal Geol.* **2018**, *199*, 39−51.

(20) Strąpoć, D.; Mastalerz, M.; Schimmelmann, A.; Drobniak, A.; Hasenmueller, N. R. Geochemical constraints on the origin and volume of gas in the New Albany Shale (Devonian−Mississippian), eastern Illinois Basin. *AAPG Bull.* **2010**, *94*, 1713−1740.

(21) Hao, F.; Zou, H.; Lu, Y. Mechanisms of shale gas storage: Implications for shale gas exploration in China. *AAPG Bull.* **2013**, *97*, 1325−1346.

(22) Qiu, Z.; Zou, C.; Wang, H.; Dong, D.; Lu, B.; Chen, Z.; Liu, D.; Li, G.; Liu, H.; He, J.; Wei, L. Discussion on the characteristics and controlling factors of differential enrichment of shale gas in the Wufeng-Longmaxi formations in south China. *J. Nat. Gas Geosci.* **2020**, *5*, 117−128.

(23) Schieber, J.. SEM observations on ion-milled samples of Devonian black shales from Indiana and New York: the petrographic context of multiple pore types. In *Electron Microscopy of Shale Hydrocarbon Reservoirs*; Camp, W., Diaz, E., Wawak, B., Eds.; American Association of Petroleum Geologists (AAPG): Tulsa, OK, 2013, AAPG Memoir, Vol. *102*; pp 153−171.

(24) Curtis, M. E.; Cardott, B. J.; Sondergeld, C. H.; Rai, C. S. Development of organic porosity in the Woodford Shale with increasing thermal maturity. *Int. J. Coal Geol.* **2012**, *103*, 26−31.

(25) Schieber, J.; Lazar, R.; Bohacs, K.; Klimentidis, R.; Dumitrescu, M.; Ottmann, J. An SEM study of porosity in the Eagle Ford Shale of Texas—Pore types and porosity distribution in a depositional and sequence-stratigraphic Context. In *The Eagle Ford Shale: A*

Renaissance in U.S. Oil Production; Breyer, J. A., Ed.; American Association of Petroleum Geologists (AAPG): Tulsa, OK, 2016; AAPG Memoir, Vol. *110*, pp 167−186.

(26) Chalmers, G. R.; Bustin, R. M.; Power, I. M. Characterization of gas shale pore systems by porosimetry, pycnometry, surface area, and field emission scanning electron microscopy/transmission electron microscopy image analyses: Examples from the Barnett, Woodford, Haynesville, Marcellus, and Doig units. *AAPG Bull.* **2012**, *96*, 1099−1119.

(27) Mastalerz, M.; He, L.; Melnichenko, Y. B.; Rupp, J. A. Porosity of coal and shale: Insights from gas adsorption and SANS/USANS techniques. *Energy Fuels* **2012**, *26*, 5109−5120.

(28) Bousige, C.; Ghimbeu, C. M.; Vix-Guterl, C.; Pomerantz, A. E.; Suleimenova, A.; Vaughan, G.; Garbarino, G.; Feygenson, M.; Wildgruber, C.; Ulm, F.-J.; Pellenq, R. J.-M.; Coasne, B. Realistic molecular model of kerogen's nanostructure. *Nat. Mater.* **2016**, *15*, 576−582.

(29) Sun, M.; Zhao, J.; Pan, Z.; Hu, Q.; Yu, B.; Tan, Y.; Sun, L.; Bai, L.; Wu, C.; Blach, T. P.; Zhang, Y.; Zhang, C.; Cheng, G. Pore characterization of shales: A review of small angle scattering technique. *J. Nat. Gas Sci. Eng.* **2020**, *78*, 103294.

(30) Chen, J.; Xiao, X. Evolution of nanoporosity in organic-rich shales during thermal maturation. *Fuel* **2014**, *129*, 173−181.

(31) Rexer, T. F.; Mathia, E. J.; Aplin, A. C.; Thomas, K. M. High-pressure methane adsorption and characterization of pores in Posidonia shales and isolated kerogens. *Energy Fuels* **2014**, *28*, 2886−2901.

(32) Ko, L. T.; Loucks, R. G.; Zhang, T.; Ruppel, S. C.; Shao, D. Pore and pore network evolution of Upper Cretaceous Boquillas (Eagle Ford-equivalent) mudrocks: Results from gold tube pyrolysis experiments. *AAPG Bull.* **2016**, *100*, 1693−1722.

(33) Ko, L. T.; Ruppel, S. C.; Loucks, R. G.; Hackley, P. C.; Zhang, T.; Shao, D. Pore-types and pore-network evolution in Upper Devonian-Lower Mississippian Woodford and Mississippian Barnett mudstones: Insights from laboratory thermal maturation and organic petrology. *Int. J. Coal Geol.* **2018**, *190*, 3−28.

(34) Dong, T.; Harris, N. B. The effect of thermal maturity on porosity development in the Upper Devonian -Lower Mississippian Woodford Shale, Permian Basin, US: Insights into the role of silica nanospheres and microcrystalline quartz on porosity preservation. *Int. J. Coal Geol.* **2020**, *217*, 103346.

(35) Hackley, P. C.; Cardott, B. J. Application of organic petrography in North American shale petroleum systems: A review. *Int. J. Coal Geol.* **2016**, *163*, 8−51.

(36) Mastalerz, M.; Drobniak, A.; Stankiewicz, A. B. Origin, properties, and implications of solid bitumen in source-rock reservoirs: A review. *Int. J. Coal Geol.* **2018**, *195*, 14−36.

(37) Liu, B.; Schieber, J.; Mastalerz, M. Petrographic and micro-FTIR study of organic matter in the Upper Devonian New Albany Shale during thermal maturation: Implications for kerogen transformation. In *Mudstone Diagenesis: Research Perspectives for Shale Hydrocarbon Reservoirs, Seals, and Source Rocks*; Camp, W., Milliken, K., Taylor, K., Fishman, N., Hackley, P., Macquaker, J., Eds.; American Association of Petroleum Geologists (AAPG), AAPG Memoir: Tulsa, OK, 2019; Vol. *120*, pp 165−188.

(38) Sanei, H. Genesis of solid bitumen. *Sci. Rep.* **2020**, *10*, 1−10.

(39) Bjørlykke, K. Clay mineral diagenesis in sedimentary basins—a key to the prediction of rock properties. Examples from the North Sea Basin. *Clay Miner.* **1998**, *33*, 15−34.

(40) Lazar, O. R. Redefinition of the New Albany Shale of the Illinois Basin: An integrated, stratigraphic, sedimentologic, and geochemical study. Ph.D. Thesis, Indiana University Bloomington, 2007, p 336.

(41) Liu, B.; Schieber, J.; Mastalerz, M.; Teng, J. Organic matter content and type variation in the sequence stratigraphic context of the Upper Devonian New Albany Shale, Illinois Basin. *Sediment. Geol.* **2019**, *383*, 101−120.

(42) ASTM. D2797 Standard practice for preparing coal samples for microscopical analysis by reflected light. In *Petroleum Products, Lubricants, and Fossil Fuels; Gaseous Fuels; Coal and Coke*; ASTM International: West Conshohocken, PA, 2015, Sec. 5, V. 05.06.

(43) Bish, D. L.; Post, J. E. Quantitative mineralogical analysis using the Rietveld full-pattern fitting method. *Am. Mineral.* **1993**, *78*, 932−940.

(44) Vandenbroucke, M.; Largeau, C. Kerogen origin, evolution and structure. *Org. Geochem.* **2007**, *38*, 719−833.

(45) Wei, L.; Mastalerz, M.; Schimmelmann, A.; Chen, Y. Influence of Soxhlet-extractable bitumen and oil on porosity in thermally maturing organic-rich shales. *Int. J. Coal Geol.* **2014**, *132*, 38−50.

(46) Rouquerol, J.; Avnir, D.; Fairbridge, C. W.; Everett, D. H.; Haynes, J. M.; Pernicone, N.; Ramsay, J. D. F.; Sing, K. S. W.; Unger, K. K. Recommendations for the characterization of porous solids (Technical Report). *Pure Appl. Chem.* **1994**, *66*, 1739−1758.

(47) Mastalerz, M.; Hampton, L.; Drobniak, A.; Loope, H. Significance of analytical particle size in low-pressure N2 and CO2 adsorption of coal and shale. *Int. J. Coal Geol.* **2017**, *178*, 122−131.

(48) Brunauer, S.; Emmett, P. H.; Teller, E. Adsorption of gases in multimolecular layers. *J. Am. Chem. Soc.* **1938**, *60*, 309−319.

(49) Rouquerol, F.; Rouquerol, J.; Sing, K. S. W.; Llewellyn, P.; Maurin, G. *Adsorption by Powders and Porous Solids: Principles, Methodology and Applications*, 2nd ed.; Academic Press: Oxford, 2014; pp 159−189.

(50) Harkins, W. D.; Jura, G. Surfaces of solids. XIII. A vapor adsorption method for the determination of the area of a solid without the assumption of a molecular area, and the areas occupied by nitrogen and other molecules on the surface of a solid. *J. Am. Chem. Soc.* **1994**, *66*, 1366−1373.

(51) Barrett, E. P.; Joyner, L. G.; Halenda, P. P. The determination of pore volume and area distributions in porous substances. I. Computations from nitrogen isotherms. *J. Am. Chem. Soc.* **1951**, *73*, 373−380.

(52) Liu, B.; Schieber, J.; Mastalerz, M.; Teng, J. Variability of rock mechanical properties in the sequence stratigraphic context of the Upper Devonian New Albany Shale, Illinois Basin. *Mar. Petrol. Geol.* **2020**, *112*, 104068.

(53) Bruner, K. R.; Walker-Milani, M.; Smosna, R. Lithofacies of the Devonian Marcellus Shale In the Eastern Appalachian Basin, U.S.A. *J. Sediment. Res.* **2015**, *85*, 937−954.

(54) Mastalerz, M.; Schimmelmann, A.; Lis, G. P.; Drobniak, A.; Stankiewicz, A. Influence of maceral composition on geochemical characteristics of immature shale kerogen: Insight from density fraction analysis. *Int. J. Coal Geol.* **2012**, *103*, 60−69.

(55) Liu, B.; Mastalerz, M.; Schieber, J.; Teng, J. Association of uranium with macerals in marine black shales: Insights from the Upper Devonian New Albany Shale, Illinois Basin. *Int. J. Coal Geol.* **2020**, *217*, 103351.

(56) Liu, B.; Teng, J.; Mastalerz, M.; Schieber, J. Assessing the thermal maturity of black shales using vitrinite reflectance: Insights from Devonian black shales in the eastern United States. *Int. J. Coal Geol.* **2020**, *220*, 103426.

(57) Teng, J.; Mastalerz, M.; Liu, B.; Gognat, T.; Hauser, E.; McLaughlin, P. Variations of organic matter transformation in response to hydrothermal fluids: Example from the Indiana part of the Illinois Basin. *Int. J. Coal Geol.* **2020**, *219*, 103410.

(58) Frost, J. K.; Shaffer, N. R. Mineralogy and geochemistry. In *Gas Potential of the New Albany Shale (Devonian and Mississippian) in the Illinois Basin*; Hasenmueller, N. R., Comer, J. B., Eds.; Gas Research Institute, GRI-00/0068; Illinois Basin Studies, 1994; Vol. *2*, pp 41−45.

(59) Durand, B.; Monin, J. C. Elemental analysis of kerogens (C, H, O, N, S, Fe). In *Kerogen: Insoluble Organic Matter from Sedimentary Rocks*; Durand, B., Ed.; Editions: Technip: Paris, 1980; pp 113−142.

(60) Suárez-Ruiz, I.; Flores, D.; Mendonça Filho, J. G.; Hackley, P. C. Review and update of the applications of organic petrology: Part 1, geological applications. *Int. J. Coal Geol.* **2012**, *99*, 54−112.

(61) Camp, W. K. Diagenetic evolution of organic matter cements: Implications for unconventional shale reservoir quality prediction. In *Mudstone Diagenesis: Research Perspectives for Shale Hydrocarbon*

Reservoirs, Seals, and Source Rocks; Camp, W., Milliken, K., Taylor, K., Fishman, N., Hackley, P., Macquaker, J., Eds.; American Association of Petroleum Geologists (AAPG), AAPG Memoir: Tulsa, OK, 2019; Vol. *120*, pp 209−224.

(62) Bernard, S.; Wirth, R.; Schreiber, A.; Schulz, H.-M.; Horsfield, B. Formation of nanoporous pyrobitumen residues during maturation of the Barnett Shale (Fort Worth Basin). *Int. J. Coal Geol.* **2012**, *103*, 3−11.

(63) Cardott, B. J.; Landis, C. R.; Curtis, M. E. Post-oil solid bitumen network in the Woodford Shale, USA - A potential primary migration pathway. *Int. J. Coal Geol.* **2015**, *139*, 106−113.

(64) Ko, L. T.; Loucks, R. G.; Ruppel, S. C.; Zhang, T.; Peng, S. Origin and characterization of Eagle Ford pore networks in the south Texas Upper Cretaceous shelf. *AAPG Bull.* **2017**, *101*, 387−418.

(65) Cardott, B. J.; Curtis, M. E. Identification and nanoporosity of macerals in coal by scanning electron microscopy. *Int. J. Coal Geol.* **2018**, *190*, 205−217.

(66) Ardakani, O. H.; Sanei, H.; Ghanizadeh, A.; Lavoie, D.; Chen, Z.; Clarkson, C. R. Do all fractions of organic matter contribute equally in shale porosity? A case study from Upper Ordovician Utica Shale, southern Quebec, Canada. *Mar. Pet. Geol.* **2018**, *92*, 794−808.

(67) Craddock, P. R.; Haecker, A.; Bake, K. D.; Pomerantz, A. E. Universal curves describing the chemical and physical evolution of type II kerogen during thermal maturation. *Energy Fuels* **2020**, *34*, 15217−15233.

(68) Mondol, N. H.; Bjørlykke, K.; Jahren, J.; Høeg, K. Experimental mechanical compaction of clay mineral aggregates-Changes in physical properties of mudstones during burial. *Mar. Pet. Geol.* **2007**, *24*, 289−311.

(69) Barth, T.; Bjørlykke, K. Organic acids from source rock maturation: generation potentials, transport mechanisms and relevance for mineral diagenesis. *Appl. Geochem.* **1993**, *8*, 325−337.

(70) Sondergeld, C. H.; Newsham, K. E.; Comisky, J. T.; Rice, M. C.; Rai, C. S. Petrophysical considerations in evaluating and producing shale gas resources. In SPE Unconventional Gas Conference; Society of Petroleum Engineers: Pittsburgh, PA, USA, February 23−25, 2010; SPE paper 131768.

(71) Van Olphen, H.; Fripiat, J. J. *Data Handbook for Clay Minerals and Other Nonmetallic Minerals*; Pergamon Press: Oxford, 1979, pp 203−216.

(72) Pugh, C. E.; Hossner, L. R.; Dixon, J. B. Pyrite and marcasite surface area as influenced by morphology and particle diameter. *Soil Sci. Soc. Am. J.* **1981**, *45*, 979−982.

(73) Chiou, C. T.; Rutherford, D. W.; Manes, M. Sorption of nitrogen and ethylene glycol monoethyl ether (EGME) vapors on some soils, clays, and mineral oxides and determination of sample surface areas by use of sorption data. *Environ. Sci. Technol.* **1993**, *27*, 1587−1594.

(74) Ji, L.; Zhang, T.; Milliken, K. L.; Qu, J.; Zhang, X. Experimental investigation of main controls to methane adsorption in clay-rich rocks. *Appl. Geochem.* **2012**, *27*, 2533−2545.

(75) Liu, D.; Yuan, P.; Liu, H.; Li, T.; Tan, D.; Yuan, W.; He, H. High-pressure adsorption of methane on montmorillonite, kaolinite and illite. *Appl. Clay Sci.* **2013**, *85*, 25−30.

(76) Wang, Z.; Zhang, Y.; Guo, P.; Liu, H.; Liao, H. A novel method to calculate the gas adsorption of mixed minerals. *SN Appl. Sci.* **2020**, *2*, 292.

(77) Gonciaruk, A.; Hall, M. R.; Fay, M. W.; Parmenter, C. D.; Vane, C. H.; Khlobystov, A. N.; Ripepi, N. Kerogen nanoscale structure and CO_2 adsorption in shale micropores. *Sci. Rep.* **2021**, *11*, 3920.

(78) Mahajan, O. P. CO2 surface area of coals: The 25-year paradox. *Carbon* **1991**, *29*, 735−742.

(79) Rouquerol, J.; Llewellyn, P.; Rouquerol, F. Is the BET equation applicable to microporous adsorbents? In *Studies in Surface Science and Catalysis*; Llewellyn, P., Rodriguez-Reinoso, F., Rouquerol, J., Seaton, N., Eds., 2007; Vol. *160*, pp 49−56.

(80) Qiu, Z.; Liu, B.; Dong, D.; Lu, B.; Yawar, Z.; Chen, Z.; Schieber, J. Silica diagenesis in the Lower Paleozoic Wufeng and Longmaxi Formations in the Sichuan Basin, South China: Implications for reservoir properties and paleoproductivity. *Mar. Pet. Geol.* **2020**, *121*, 104594.

(81) Zhao, J.; Jin, Z.; Jin, Z.; Wen, X.; Geng, Y. Origin of authigenic quartz in organic-rich shales of the Wufeng and Longmaxi Formations in the Sichuan Basin, South China: Implications for pore evolution. *J. Nat. Gas Sci. Eng.* **2017**, *38*, 21−38.